Lift-drag and flow structures associated with the "clap and fling" motion

Nipun Arora, Amit Gupta, Sanjeev Sanghi, Hikaru Aono, and Wei Shyy

Citation: Physics of Fluids (1994-present) **26**, 071906 (2014); doi: 10.1063/1.4890221
View online: http://dx.doi.org/10.1063/1.4890221
View Table of Contents: http://scitation.aip.org/content/aip/journal/pof2/26/7?ver=pdfcov
Published by the AIP Publishing

PHYSICS OF FLUIDS **26**, 071906 (2014)

Lift-drag and flow structures associated with the "clap and fling" motion

Nipun Arora,[1] Amit Gupta,[1,a)] Sanjeev Sanghi,[2] Hikaru Aono,[3] and Wei Shyy[4]
[1]*Department of Mechanical Engineering, Indian Institute of Technology, Hauz Khas, New Delhi 110016, India*
[2]*Department of Applied Mechanics, Indian Institute of Technology, Hauz Khas, New Delhi 110016, India*
[3]*Institute of Space and Astronautical Science, Japan Aerospace Exploration Agency, Sagamihara, Kanagawa 2525210, Japan*
[4]*Department of Mechanical Engineering, Hong Kong University of Science and Technology, Clear Water Bay, Hong Kong, China*

(Received 9 November 2013; accepted 2 July 2014; published online 21 July 2014)

The present study focuses on the analysis of the fluid dynamics associated with the flapping motion of finite-thickness wings. A two-dimensional numerical model for one and two-winged "clap and fling" stroke has been developed to probe the aerodynamics of insect flight. The influence of kinematic parameters such as the percentage overlap between translational and rotational phase ξ, the separation between two wings δ and Reynolds numbers Re on the evolvement of lift and drag has been investigated. In addition, the roles of the leading and trailing edge vortices on lift and drag in clap and fling type kinematics are highlighted. Based on a surrogate analysis, the overlap ratio ξ is identified as the most influential parameter in enhancing lift. On the other hand, with increase in separation δ, the reduction in drag is far more dominant than the decrease in lift. With an increase in Re (which ranges between 8 and 128), the mean drag coefficient decreases monotonously, whereas the mean lift coefficient decreases to a minimum and increases thereafter. This behavior of lift generation at higher Re was characterized by the "wing-wake interaction" mechanism which was absent at low Re. © *2014 AIP Publishing LLC*. [http://dx.doi.org/10.1063/1.4890221]

I. INTRODUCTION

MICRO-Air-Vehicles (MAVs) have aroused a substantial and rapidly growing interest among many researchers and engineers in the aerospace community. These miniaturized aerial vehicles are symbolized by their small size (<15 cm) and low flight speed (10–20 m/s).[1] MAVs armed with video cameras, transmitters, and sensors, can perform surveillance, remote sensing, spying, and reconnaissance operations in small or closed spaces (in buildings, tunnels, etc.) and possess a very promising future in defense and military applications.[2] There are two prominent features of MAV flight: (i) low Reynolds number $O(10^4)$, resulting in unfavorable aerodynamic conditions (such as low lift to drag ratio), and (ii) small physical dimensions, resulting in favorable scaling characteristics including structural strength, reduced stall speed, and low inertia.[3–5]

In general, there are three concepts that can be used in the design of the MAVs: fixed-wing, rotary-wing and flapping-wing. Fixed wing MAVs are difficult to maneuver in confined spaces, are not swift enough to deal with obstacle avoidance, and are also incapable of hovering.[5,6] Although rotary wing flight vehicles have good hovering performance and acquire the skill of vertical take-off and landing, they are too noisy and inefficient at low Reynolds number.[6] On the contrary, flapping wing MAVs have good maneuvering and hovering capabilities as they generate their lift not from

a)Author to whom correspondence should be addressed. Electronic mail: agupta@mech.iitd.ac.in

forward airspeed of the aircraft but depending on how fast their wings are flapped.[3–9] Moreover, operating at such low speeds flapping wings require the least specific power in comparison to the fixed or rotary wings.[10] Hence, the above stated advantages make flapping flight an ideal choice for designing MAVs.

The aerial flapping flight of birds and insects and the guiding principles in nature have provided scientists a general design principle to develop MAVs as they share similar dimensions, weight, flight speed, and flight environment.[3,4,6,11] Biological flyers represent some of the nature's finest examples of locomotion in terms of efficiently maneuvering the body through space, navigation, and control capabilities.[3] Fundamentally, the difference is the Reynolds number range of birds (except for hummingbirds, $O(10^4)$ or higher) and insects (typically $O(10^2–10^3)$). The wing structure of insects is lighter than the birds which make them more suitable for designing MAVs.[6]

Pioneering work on flapping aerodynamics of insects was done by Weis-Fogh[12] who examined the hovering motion of tiny wasp *Encarsia formosa* and suggested an innovative theory (known as Weis-Fogh mechanism) based on the "clap and fling" motion that enhanced lift[13,14] overcoming the *Wagner Effect*. When an inclined wing begins to flap from rest, the circulation around the wing goes through a transient phase before achieving steady state. As the wing begins to flap, vorticity is generated at the trailing edge of the wing. This vorticity rolls up into a starting vortex which interferes with the circulation that grows around the wing and hence leads to a reduction in the forces.[11–15] As the starting vortex moves further and further away from the wing, its influence on the wing circulation falls. This delay in development of circulation around the wing is known as *Wagner Effect*. However, during the "clap" (dorsal touching of the two leading edges towards the end of upstroke), the oppositely directed circulations of the two wings annul each other, thereby weakening the trailing edge vortex generated by each wing on the next stroke.[11–15] This allows rapid build-up of circulation around the wings and thus extends the benefit of lift with time without any delay. After the clap, the leading edges of the wings "fling" apart causing the surrounding fluid to rush into the intervening low pressure space. This further leads to build up of circulation and a higher lift. The wings then move away from each other with oppositely directed circulations.

The most prevalent aerodynamic phenomenon associated with the flapping flight that leads to enhancement of lift or thrust is the leading edge vortex (LEV), also known as *delayed stall* or *dynamic stall* mechanism.[15–20] The leading edge vortex produces a suction force which supplements the force exerted on the wing by the downward motion of the fluid stream. These stabilized LEVs are responsible for large circulatory forces generated transiently during the upstroke and downstroke. In addition to the LEVs, another unsteady mechanism that can significantly contribute to lift generation is wing-wake interaction.[3–5,11,15,19–22] If the flapping frequency is high, the wings may interact with the leading and trailing edge vortices that were shed in the previous strokes. The shed vortices induce strong velocity and acceleration between them with which the wing interacts leading to an increase in the aerodynamic forces immediately after stroke reversal.

With recent advances in computational methods, numerical simulations have been performed by various researchers[22–39] to investigate the fluid physics that emanates from the flapping motion of a wing. These have primarily relied on employing the Navier-Stokes equation based macroscopic methods which have been successful to an extent. Liu *et al.*[24] developed a three-dimensional model to study the unsteady aerodynamics of a hovering hawk-moth. During the translation phase, a leading edge vortex with axial flow along the span of the wing, which creates a negative pressure region and led to lift enhancement, was detected. Further investigation showed that the LEV was substantially deformed during pitching and was shed before subsequent translational motion. Miller and Peskin[26] have used the immersed boundary method to solve the two-dimensional Navier-Stokes equations for two wings performing an idealized "clap and fling" stroke and a "fling" half stroke. The instantaneous lift coefficient per wing, as a function of time, was calculated for a range of Reynolds numbers between 8 and 128. Their results showed that the lift coefficient for two-winged fling during the translational phase was about 70% higher than the one-winged fling. In addition, lift enhancement increased with decreasing Re suggesting that the Weis-Fogh mechanism of lift generation has greater benefit to insects flying at lower Re. A comparison of the mean lift recorded during separate "fling" and "clap and fling" strokes showed that a higher lift was registered for the latter case and was accredited to wing-wake interaction. Moreover, it was identified that the difference between the

mean lift recorded for the two cases increases with an increase in Re, signifying that the wing-wake effect dominates only at higher Re. Using a moving overset grid method, Sun and Yu[27] investigated the effect of separation between wings performing a three-dimensional "clap and fling" motion for Re = 15.3. They also discussed that the interaction between wings for a particular overlap may lead to significant enhancement in average lift by as much as 20%. Kolomenskiy *et al.*[28] used a two-dimensional Fourier pseudo-spectral method with volume penalization to determine the variation in lift for Re = 128. In later studies, Kolomenskiy *et al.*[29,30] conducted two- and three-dimensional simulations for the "clap-fling-sweep" model. Using two-dimensional simulations for Re < 20, they investigated the fluid mechanics emanating close to the hinge point near the time instant when the wings begin "sweep" at the end of "fling" phase. Their three-dimensional simulations for Re of 128 and 1400 showed that the two-dimensional approximation is justified during the fling kinematics. Trizila *et al.*[31] numerically investigated the two- and three-dimensional low aspect ratio (AR = 4) hovering airfoil aerodynamics at Re = 100. Their study revealed that, in addition to the leading edge vortex and wake-capture mechanisms, a persistent jet induced by the shed vortices in the wake can significantly influence the lift and power performance. Sun and Tang[33] developed a computational model to examine the flapping motion of a fruit fly in normal hovering mode. Their work indicated that rapid acceleration or rotation have a strong influence on instantaneous lift peaks which rise when translation or rotation rate are higher; however, no comment was made regarding mean lift.

However, considerable challenges, such as the development of robust and computationally efficient schemes of re-meshing, grid generation, efficient matrix solvers, etc., still exist. In the past two decades, the lattice Boltzmann method (LBM) has been presented as an alternative framework compared to the Navier-Stokes simulations. Some of the salient features of LBM are: (a) the solution method is local in nature and hence there is no requirement of solving simultaneous linear algebraic equations which makes the solution process non-iterative and free of matrix inversions, (b) it is easy to implement and parallelize, and (c) LBM employs a stationary mesh for both fixed and moving boundary problems.

In a recent work, Lu and co-workers[34] studied the aerodynamics of a two-dimensional two-winged insect hovering using LBM and examined the effect of Reynolds number (25–200), stroke amplitude, angle of attack, and flight environment (ground clearance) on unsteady forces and vortical structures. It was shown that the time-averaged vertical and horizontal forces were weakly dependent on the stroke amplitude as it varied from 3.0 to 5.0, corresponding to the range of amplitude-to-chord ratio employed in small insect flight. However, changing the attack angle was shown to lead to an appreciable change in mean drag and lift coefficients, with the mean lift coefficient reaching its maximum at 45°. In separate studies, they have also investigated the ground effect on insect hovering using a two-dimensional immersed boundary LBM by examining normal and dragonfly hovering modes at Re = 100.[38,39] They showed that, in the normal hovering mode, the symmetry of the flow field is destroyed when the foil moves away from the ground, and the back-stroke is the major contributor to the vertical force.

Despite all these studies, the interplay of rotational and translational motion, the initial separation between wings and the flight Reynolds number has not been addressed. In this work, we carry forward from the modeling efforts of Liu *et al.*[34] and develop a two-dimensional "clap and fling" model for one and two wings of finite thicknesses to deduce the impact of kinematic parameters, namely, wing separation δ, translational-rotational percentage overlap ξ, and Reynolds number Re, on evolution of lift and drag. To the best of our knowledge, development of reduced-order models and determining the relative impact of each of these variables on aerodynamic forces has not been pursued so far. Due to the advantages associated with LBM in handling moving boundary problems, in the present study a lattice Boltzmann framework to analyze the flapping motion of wings employing the "clap and fling" kinematics will be developed. In particular, we focus on the following objectives in this study.

1. Quantify the dependence of average lift and drag on the percentage overlap of rotational and translational motion ξ, Reynolds number and separation between two wings δ.

2. Formulate reduced-order models through surrogate modeling and identify the relationship between the mean lift and system parameters (δ, ξ, and Re). These models can offer fast prediction of mean lift and identify regions that critically affect performance, and
3. Ascertain the relative importance of the three kinematic parameters that can help elucidate their interplay associated with flapping wings that contribute to generation of lift in clap-and-fling.

II. PROBLEM DESCRIPTION

A. Clap and fling motion

An idealized wing kinematic model was proposed by Miller and Peskin,[26] modeled after a physical experiment of Dickinson and Gotz.[18] This model was carried out to study flight dynamics similar to that of a small insect *Drosophila melanogaster* to define the "clap and fling" motion. It composed of "downstroke," "supination," "upstroke," and "pronation" phases in sequence.[11,15,26] The ventral to dorsal and dorsal to ventral motion of the wing is known as "upstroke" and "downstroke," respectively. "Supination" refers to the rotational transition from downstroke to upstroke that causes the ventral side to face upward. "Pronation" is the opposite of "supination" that results in ventral side facing downward during transition from upstroke to downstroke.

Fig. 1 shows a sketch of two wings where C is the chord length of the wing and D is the edge to edge distance between two wings. The physical dimensions and velocity range was chosen to match those of Miller and Peskin's[26] computational study. C was taken as 0.05 m and the aspect ratio (chord length to thickness ratio) of the wing was set as 10 for all simulations. Miller and Peskin[26] have stated that their aim was not just to emulate the previous work related to clap and fling but to further explore the impact of lowering down the Reynolds number to that of smallest flying insects ($\sim$Re $= 6$) employing the same kinematics. The range of translational velocities for insect flight varied from 0.00375 to 0.06 m/s in their computational study.[26] In this work, maximum translational velocity V (as discussed later) was taken as 0.00774 m/s and the angle of attack ($\Delta\theta$) was held at 45° as lift was reported to be maximum at this angle.[34]

The following non-dimensional parameters can be introduced to conduct a parametric analysis of clap-and-fling kinematics. δ is defined as

$$\delta = \frac{D}{C}, \tag{1}$$

i.e., the gap between the two wings D is expressed in terms of fraction of chord length C.

Reynolds number is defined as

$$\mathrm{Re} = \frac{VC}{\nu}, \tag{2}$$

where ν is the kinematic viscosity of the fluid.

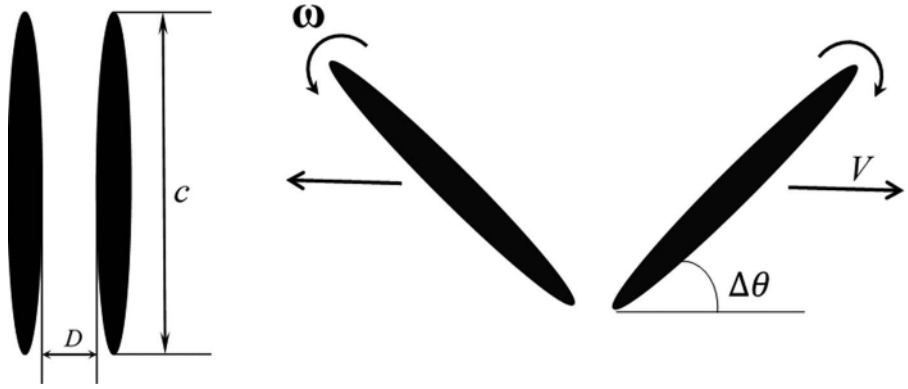

FIG. 1. Layout of the two wings of chord length C with the translational velocity V, angular velocity $\boldsymbol{\omega}$ and angle of attack $\Delta\theta$.

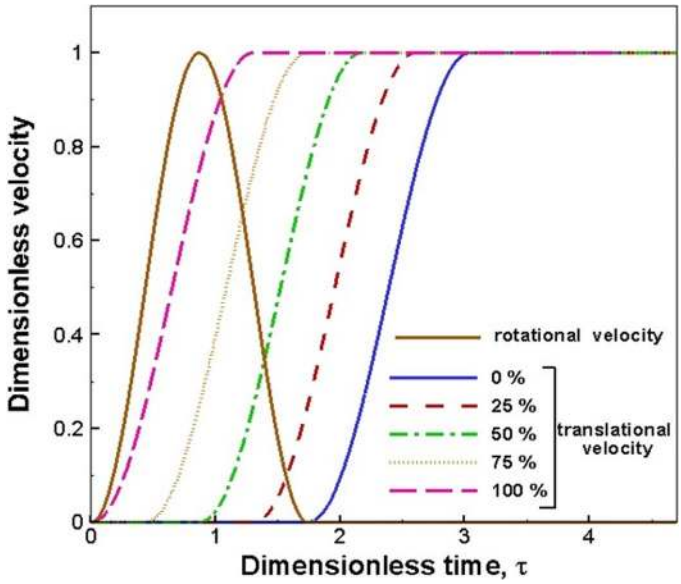

FIG. 2. The dimensionless rotational and translational velocities (non-dimensionalized by their respective maximum velocities) as a function of dimensionless time for different overlaps for fling half-stroke.

The translational rotational overlap ξ is defined as the percentage of the rotation phase in which translation also occurs. This has been explained for fling half stroke (excluding the deceleration portion of the translational velocity) through Fig. 2. For 0% overlap, translation begins after the rotation is completed. For 100% overlap, the rotation and translation start simultaneously.

The kinematic model to study one complete cycle of "clap and fling" motion was recreated. The kinematics and the motion of the right wing undergoing "clap and fling" is described here. The kinematics and the motion of the left wing, as obvious, is the mirror image of that of the right wing.

As shown in Fig. 3, the translational phase was divided into three stages in sequence: translational acceleration, steady translation with a fixed velocity V and attack angle $\Delta\theta$ (as indicated in Fig. 1),

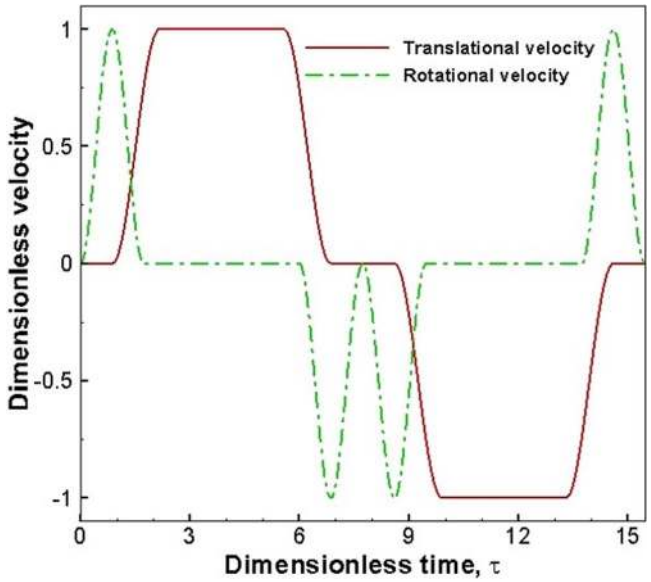

FIG. 3. The dimensionless translational and rotational velocities of the right wing as a function of dimensionless time for entire "clap and fling" cycle for $\xi = 50\%$.

and translational deceleration. The translational velocity for the right wing as a function of overlap ξ with reference to Fig. 3 and dimensionless time, τ, can be written as

$$\mathbf{v}(\tau)=\begin{cases}0, & 0\le\tau<\tau_{acc,f}\\ \frac{V}{2}\left\{1+\cos\left[\pi+\frac{\pi\left(\tau-\tau_{acc,f}\right)}{\Delta\tau_{acc}}\right]\right\}, & \tau_{acc,f}\le\tau<\tau_{acc,f}+\Delta\tau_{acc}\\ V, & \tau_{acc,f}+\Delta\tau_{acc}\le\tau<\tau_{dec,f}\\ \frac{V}{2}\left\{1-\cos\left[\pi+\frac{\pi\left(\tau-\tau_{dec,f}\right)}{\Delta\tau_{dec}}\right]\right\}, & \tau_{dec,f}\le\tau<\tau_{dec,f}+\Delta\tau_{dec}\\ 0, & \tau_{dec,f}+\Delta\tau_{dec}\le\tau<\tau_{acc,c}\\ -\frac{V}{2}\left\{1+\cos\left[\pi+\frac{\pi\left(\tau-\tau_{acc,c}\right)}{\Delta\tau_{acc}}\right]\right\}, & \tau_{acc,c}\le\tau<\tau_{acc,c}+\Delta\tau_{acc}\\ -V, & \tau_{acc,c}+\Delta\tau_{acc}\le\tau<\tau_{dec,c}\\ -\frac{V}{2}\left\{1-\cos\left[\pi+\frac{\pi\left(\tau-\tau_{dec,c}\right)}{\Delta\tau_{dec}}\right]\right\}, & \tau_{dec,c}\le\tau<\tau_{dec,c}+\Delta\tau_{dec}\\ 0, & \tau_{dec,c}+\Delta\tau_{dec}\le\tau\le T\end{cases}, \quad (3)$$

where τ is the dimensionless time defined by $\tau = tV/C$, t is the dimensional time, τ_{acc} (or τ_{dec}) is the dimensionless time when translational acceleration (or deceleration) begins (subscripts c and f represent clap and fling, respectively), $\Delta\tau_{acc}$(or $\Delta\tau_{dec}$) is the dimensionless duration of translational acceleration (or deceleration) and $\Delta\tau_s$ is the dimensionless duration of the steady translation and was fixed as 3.4 for all overlaps. Also, $\tau_{acc,f} = (1-\xi)\Delta\tau_{rot}$, $\tau_{dec,f} = \tau_{acc,f} + \Delta\tau_{acc} + \Delta\tau_s$, $\tau_{acc,c} = T/2 + (1-\xi)\Delta\tau_{rot}$, and $\tau_{dec,c} = \tau_{acc,c} + \Delta\tau_{acc,c} + \Delta\tau_s$. The dimensionless duration of one complete cycle, T, is defined as

$$T = 2[2\Delta\tau_{rot}(1-\xi) + \Delta\tau_{acc} + \Delta\tau_s + \Delta\tau_{dec}]. \quad (4)$$

During the rotational phase, the wings rotate about the leading or the trailing edges. The angular velocity (clockwise is positive and anticlockwise is negative) as a function of dimensionless time τ of the right wing is given by

$$\boldsymbol{\omega}(\tau)=\begin{cases}\frac{\omega_{rot}}{2}\left\{1-\cos\left[2\pi\left(\frac{\tau-\tau_{turn,1}}{\Delta\tau_{rot}}\right)\right]\right\}, & 0\le\tau<\Delta\tau_{rot}\\ 0, & \Delta\tau_{rot}\le\tau<\frac{T}{2}-\Delta\tau_{rot}\\ -\frac{\omega_{rot}}{2}\left\{1-\cos\left[2\pi\left(\frac{\tau-\tau_{turn,2}}{\Delta\tau_{rot}}\right)\right]\right\}, & \frac{T}{2}-\Delta\tau_{rot}\le\tau<\frac{T}{2}\\ -\frac{\omega_{rot}}{2}\left\{1-\cos\left[2\pi\left(\frac{\tau-\tau_{turn,3}}{\Delta\tau_{rot}}\right)\right]\right\}, & \frac{T}{2}\le\tau<\frac{T}{2}+\Delta\tau_{rot}\\ 0, & \frac{T}{2}+\Delta\tau_{rot}\le\tau<T-\Delta\tau_{rot}\\ \frac{\omega_{rot}}{2}\left\{1-\cos\left[2\pi\left(\frac{\tau-\tau_{turn,4}}{\Delta\tau_{rot}}\right)\right]\right\}, & T-\Delta\tau_{rot}\le\tau\le T\end{cases}, \quad (5)$$

where

$$\omega_{rot} = \frac{2\Delta\theta\, V}{\Delta\tau_{rot} C} \quad (6)$$

is a constant determined by the total angle of rotation or attack angle ($\Delta\theta$) and by the dimensionless duration of the rotation phase ($\Delta\tau_{rot}$). Also, τ_{turn} is the dimensionless time at which rotation began (where $\tau_{turn,1} = 0$, $\tau_{turn,2} = T/2 - \Delta\tau_{rot}$, $\tau_{turn,3} = T/2$, and $\tau_{turn,4} = T - \Delta\tau_{rot}$).

Sun and Tang[33] have studied the effect of changing $\Delta\tau_{rot}$, by choosing different values of 2.3 and 3.5, and, $\Delta\tau_{acc}$ (or $\Delta\tau_{dec}$) by varying it between 1.14, 1.74, and 2.6. However, as was used in Ref. 26, $\Delta\tau_{acc}$ and $\Delta\tau_{dec}$ were taken to be 1.3 and $\Delta\tau_{rot}$ was set as 1.74 in the present study. Therefore, T was calculated to be 18.96, 17.22, 15.48, 13.74, and 12 for $\xi = 0\%$, 25%, 50%, 75%, and 100%, respectively.

One of the important parameters associated with flapping flight is the reduced frequency which is defined as $k = 2\pi f\, C\,/\,V$ where f is the frequency of clap-fling, C is the chord, and V is the maximum translational velocity. It can be shown that the reduced frequency is related to the non-dimensional cycle duration by the relationship $k = 2\pi/T$. Hence, the overlap ratio ξ should be considered as a direct measure of the reduced frequency. In the present study, the reduced frequency varies between 0.33 and 0.52 as ξ is varied from 0% to 100%.

B. Motion of center of mass

The kinematics described above were used to develop the motion for the center of mass of the wings employing "clap and fling" cycle. With reference to Fig. 4 for $\xi = 50\%$, the wings begin to rotate about their respective trailing edges in clockwise direction (i). In (ii), the rotational phase has finished. The wings are in pure translational phase and moving away from each other (ii)–(iii). In (iv), the wings are decelerating and the rotation in anticlockwise direction about the trailing edges has begun. In (v), translation has stopped, whereas the wings are still rotating till they reach a vertical orientation and thus complete the fling half-stroke. Subsequently, the wings start to undergo the clap half-stroke (vi)–(x) and rotations are made about the leading edge.

The center of mass velocity as function of dimensionless time τ was calculated as

$$\mathbf{V}_{CM}(\tau) = \mathbf{v}(\tau) + \boldsymbol{\omega}(\tau) \times \mathbf{r}, \tag{7}$$

where $\mathbf{r}$ is the vector connecting the leading/trailing edge (about which rotation takes place) to the center of mass whose absolute value was equal to half chord length. In Eq. (7), during the fling half-stroke ($0 \le \tau \le T/2$), the rotation took place about the trailing edge and $\mathbf{r}$ was thus considered from the trailing edge. During the clap half-stroke ($T/2 \le \tau \le T$), the rotation took place about the leading edge and $\mathbf{r}$ was hence considered from the leading edge. $\mathbf{V}_{CM}$ (which is the same as the term $\mathbf{U}$ in Eq. (19)) was used to predict the center of mass trajectory for all time instants, thereby assisting in accounting of the boundary nodes and calculating the net force acting on the wing.

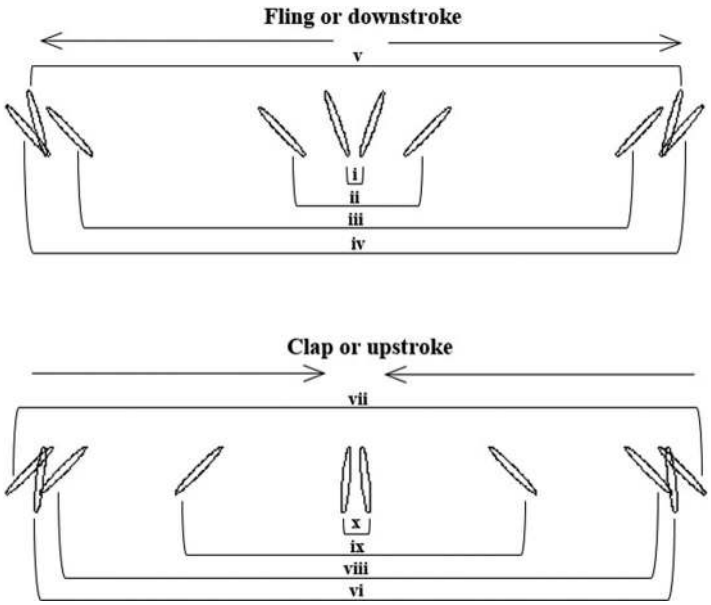

FIG. 4. The "clap and fling" motion employed by the wings for $\xi = 50\%$.

The instantaneous lift and drag coefficients for the two-dimensional motion were calculated as follows:

$$C_L = \frac{F_L}{\frac{1}{2}\rho C V^2}, \tag{8}$$

$$C_D = \frac{|F_D|}{\frac{1}{2}\rho C V^2}, \tag{9}$$

where C_L and C_D are the lift and drag coefficients per wing, respectively. F_L is the lift force per unit spanwise length, F_D is the drag force per unit spanwise length, and ρ is the density of the fluid. These time dependent forces F_L and F_D are the mean of the forces acting on two wings and were calculated by the momentum exchange method (Eq. (22)), which is discussed later. For C_D, the absolute value of force has been taken as the drag on the individual wings act in the opposite direction and their vector sum adds up to zero. Thus, their absolute values were added and averaged. For example, $|F_D| = 0.5(|F_{x,l}| + |F_{x,r}|)$ where $F_{x,l}$ and $F_{x,r}$ are the drag forces on the left and right wing, respectively.

III. NUMERICAL METHOD

A. Governing equation

The LBM is a simulation technique in which the discretized Boltzmann's equation is solved for the particle distribution function on a regular, uniform Cartesian grid. The most widely used lattice Boltzmann equation, which is a discretized version of the more general Boltzmann's equation (a function of space, time and phase space) with a single relaxation time is known as the Bhatnagar, Gross, and Krook (BGK) model.[40–45] The lattice Boltzmann equation (LBE) is given as

$$f_\alpha(\mathbf{x} + \mathbf{e}_\alpha \delta t, t + \delta t) - f_\alpha(\mathbf{x}, t) = -\frac{\left(f_\alpha(\mathbf{x}, t) - f_\alpha^{\mathrm{eq}}(\mathbf{x}, t)\right)}{\gamma} + \phi_\alpha, \tag{10}$$

where γ is dimensionless relaxation time, f_α^{eq} is the equilibrium distribution function (which depends on macroscopic properties such as density and velocity), and ϕ_α accounts for any external forces acting on the fluid. The above equation is conventionally solved in two steps,

(a) collision,

$$\tilde{f}_\alpha(\mathbf{x}, t) - f_\alpha(\mathbf{x}, t) = -\frac{\left(f_\alpha(\mathbf{x}, t) - f_\alpha^{\mathrm{eq}}(\mathbf{x}, t)\right)}{\gamma} + \phi_\alpha, \tag{11}$$

where particles arriving at a node meet and change their velocity directions.

(b) streaming,

$$f_\alpha(\mathbf{x} + \mathbf{e}_\alpha \delta t, t + \delta t) = \tilde{f}_\alpha(\mathbf{x}, t) \tag{12}$$

in which each particle travels to the neighboring node in the direction of its velocity.[42]

The equilibrium distribution function is given as

$$f_\alpha^{eq} = w_\alpha \rho \left[1 + \frac{3}{c^2}(\mathbf{e}_\alpha.\mathbf{u}) + \frac{9}{2c^4}(\mathbf{e}_\alpha.\mathbf{u})^2 - \frac{3}{2c^2}(\mathbf{u}.\mathbf{u})\right], \tag{13}$$

where w_α is a weighing factor, $\boldsymbol{e}_\alpha$ is the discrete velocity vector and c is the unit lattice speed given by $c = \delta x / \delta t$.

For the two dimensional nine-velocity model (D2Q9),

$$\mathbf{e}_\alpha = \begin{cases} (0,0), & \alpha = 0 \\ (\pm 1, 0)\, c, (0, \pm 1)c, & \alpha = 1, 2, 3, 4 \\ (\pm 1, \pm 1)\, c, & \alpha = 5, 6, 7, 8 \end{cases}. \tag{14}$$

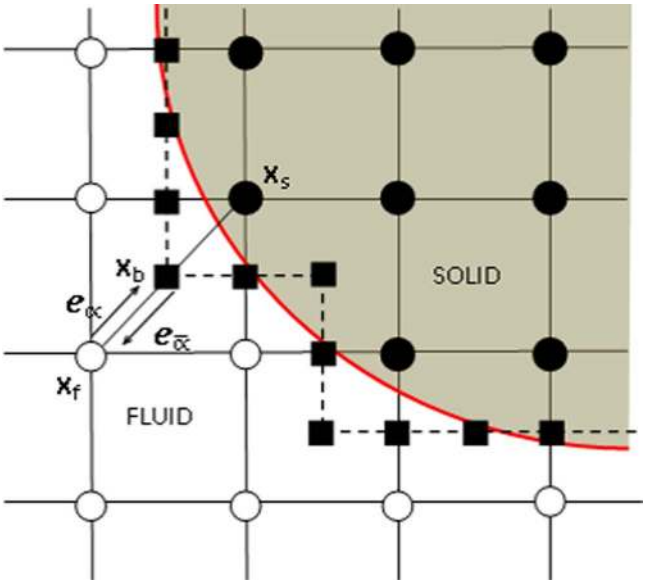

FIG. 5. Layout of the regularly spaced lattices and curved solid boundary. The hollow and filled circles denote fluid and solid nodes, respectively. The solid squares denote the boundary nodes. The dotted line represents the halfway bounceback interpretation of the curved geometry passing through the boundary nodes.

The pressure, density, and velocity can be computed from f_α as

$$p / c_s^2 = \rho = \sum_\alpha f_\alpha; \quad \rho \mathbf{u} = \sum_\alpha f_\alpha \mathbf{e}_\alpha \tag{15}$$

and the kinematic viscosity in the Navier-Stokes equation derived from the above LBE is

$$\nu = \left(\gamma - \frac{1}{2}\right) c_s^2 \delta t, \tag{16}$$

where c_s is the speed of sound and is related to lattice speed by Eq. (17),

$$c_s = \frac{1}{\sqrt{3}} c. \tag{17}$$

B. Boundary treatments

The framing of reliable boundary conditions in the BGK variant of the LBE has received considerable attention in the past.[40–42]

For the case of a moving boundary, with reference to Fig. 5, the particle surface is represented by a set of boundary nodes which lie at the mid points of the links connecting the fluid and solid nodes and the distribution functions reflected back from the solid into the fluid nodes can be written as

$$f_{\bar{\alpha}}(\mathbf{x}_f, t+1) = f_\alpha(\mathbf{x}_s, t) + 2 w_\alpha \rho \frac{3}{c^2} \mathbf{e}_{\bar{\alpha}} . \mathbf{u}_b, \tag{18}$$

where $\mathbf{e}_{\bar{\alpha}} = -\mathbf{e}_\alpha$ and $\mathbf{u}_\mathrm{b}$ is the velocity of the boundary node which is assumed to be located exactly halfway along the link between solid and fluid nodes and is given by

$$\mathbf{u}_b = \mathbf{U} + \omega \times \left(\mathbf{x} + \frac{1}{2}\mathbf{e}_\alpha - \mathbf{X}\right), \tag{19}$$

where $\mathbf{U}$ is the translational velocity of the solid, $\boldsymbol{\omega}$ is the angular velocity, and $\mathbf{X}$ is the position vector of the center of mass.

The last term in Eq. (18) accounts for the momentum transfer between the fluid and moving solid boundary.[40,43,46] However, it also introduces an extra amount of mass into the boundary node.

Consequently, with this rule the mass at the boundary node is not conserved. Ladd[40] proposed an idea of creating a fictitious fluid inside the solid object such that the lattice nodes on either side of the boundary surface are treated in an identical fashion, i.e., the fluid fills the entire domain, both inside and outside. This approach not only ensures that mass is conserved at the boundary nodes but also avoids the necessity of creating and destroying fluid as the solid particle moves (covering/uncovering the fluid/solid nodes).

With this modification, at each boundary node there are two incoming distributions $\tilde{f}_\alpha(\mathbf{x}, t)$ and $\tilde{f}_{\bar{\alpha}}(\mathbf{x}+\mathbf{e}_\alpha, t)$ from the fluid and the solid sides, respectively, corresponding to velocities $\mathbf{e}_\alpha$ and $\mathbf{e}_{\bar{\alpha}}$ along the link connecting $\mathbf{x}$ and $\mathbf{x}+\mathbf{e}_\alpha$ (as shown in Fig. 5), which are hence updated by the rule mentioned in Eq. (18) in the following manner:

$$f_\alpha(\mathbf{x}+\mathbf{e}_\alpha, t+1) = \tilde{f}_{\bar{\alpha}}(\mathbf{x}+\mathbf{e}_\alpha, t) + 2w_\alpha \rho \frac{3}{c^2}\mathbf{e}_\alpha.\mathbf{u}_b, \tag{20}$$

$$f_{\bar{\alpha}}(\mathbf{x}, t+1) = \tilde{f}_\alpha(\mathbf{x}, t) - 2w_\alpha \rho \frac{3}{c^2}\mathbf{e}_\alpha.\mathbf{u}_b. \tag{21}$$

Due to these boundary node interactions, forces are exerted on the solid which are given by

$$\mathbf{F}\left(\mathbf{x}+\frac{1}{2}\mathbf{e}_\alpha, t+\frac{1}{2}\right) = 2\left[\tilde{f}_\alpha(\mathbf{x}, t) - \tilde{f}_{\bar{\alpha}}(\mathbf{x}+\mathbf{e}_\alpha, t) - 2w_\alpha \rho \frac{3}{c^2}\mathbf{e}_\alpha.\mathbf{u}_b\right]\mathbf{e}_\alpha. \tag{22}$$

The total force $\bar{\mathbf{F}}$ on the solid object can be obtained by adding $\mathbf{F}$ over all the nodes that constitute the boundary of the object.

The overall force is calculated at the intermediate integer time step by taking the average of the total forces at half integer time steps,

$$\bar{\mathbf{F}}\left(\mathbf{x}+\frac{1}{2}\mathbf{e}_\alpha, t\right) = \frac{1}{2}\left[\bar{\mathbf{F}}\left(\mathbf{x}+\frac{1}{2}\mathbf{e}_\alpha, t-\frac{1}{2}\right) + \bar{\mathbf{F}}\left(\mathbf{x}+\frac{1}{2}\mathbf{e}_\alpha, t+\frac{1}{2}\right)\right]. \tag{23}$$

C. Surrogate modelling

Surrogate modelling involves construction of a continuous function of a set of independent variables from a limited amount of data that could have been obtained from pre-computed high fidelity simulations or physical measurements. It helps in systematically organizing simulations to ascertain the interplay between different kinematic variables. The surrogates provide fast evaluations of the various modelling and design scenarios, thereby making sensitivity and optimization studies feasible.[47]

Surrogate modelling begins by selection of the ranges (minimum and maximum values) in which the "design" or independent variables are to be studied. This process is known as setting up of design the space. Thereafter, a number of locations are chosen in this design space where numerical simulations or physical experiments will be conducted. The set of locations comprise what is known as the Design of Experiments (DOE). Once data are obtained at the selected "training" points of DOE, it is used for framing the surrogate model and carrying out the sensitivity analysis.

Surrogate models can be categorized in two groups, namely, parametric (e.g., Polynomial Response Surface, Kriging) and non-parametric (e.g., Neural Networks).[50] The surrogates constructed in this study are based on the polynomial response surface approach. In this model, the function of interest g is approximated as a linear combination of polynomial functions of design variables $\mathbf{y}$,[47,48]

$$g(\mathbf{y}) = \sum_i \beta_i a_i(\mathbf{y}) + \varepsilon, \tag{24}$$

where β_i is estimated through a least-squares method so as to minimize the variance, $a_i(\mathbf{y})$ are basis functions, i is the number of terms which depend on the degree of PRS chosen and the errors $\in$ have an expected value equal to zero. The adjusted coefficient of multiple determination (R^2_{adj}) quantifies the prediction capability of the polynomial response surface approximation.[49] A good polynomial fit should have an R^2_{adj} value close to 1.

Sensitivity analysis is usually performed to examine the influence of design parameters and is quite useful in assessing their hierarchical order of importance on the dependent variable.[31,47] It also helps in measuring the extent of interaction among the design variables.[31] In the present study, a method based on the contribution of the design variables to the variance of the objective function has been implemented.[47] There are two sensitivity indices, namely, (a) main and (b) total sensitivity. The former is a measure of the effect of individual parameters on the change in output, whereas the latter indicates the combined or collective impact of the design variables in the output variation.

IV. VALIDATION OF LBM SIMULATIONS

A. Neutrally buoyant cylinder placed off-center in shear flow

To justify the applicability of the LBM for moving boundary simulations, validation was performed for a simple case of a circular cylinder in shear flow. The motion of neutrally buoyant ($\rho_s = \rho_f$) circular cylinder initially placed at $y = 0.25$ H with the upper and lower walls moving in opposite directions at velocity $U_w/2$ for $Re = 0.625$ with confinement ratio $H/a = 8$ was studied.[51] For this case, Reynolds number is defined as $Re = Ga^2/\nu$, where "G" is the shear rate ($G = U_w/H$), "a" is the radius of cylinder and "ν" is the kinematic viscosity of the fluid.[51] The schematic diagram of the problem solved is shown in Fig. 6. Owing to the non-uniform velocity distribution in flow, pressure difference is created above and below the cylinder. This causes it to move towards the centerline of the domain after which it ceases to travel in the vertical direction. Fig. 7 compares the vertical trajectory between the present study and Feng and Michaelides[51] as the cylinder moves towards the centerline of the domain vs. the non-dimensional time *Gt*. Fig. 8 compares the two components of the dimensionless cylinder translational velocity (where U_P and V_P is the dimensional horizontal and vertical velocity, respectively) between the present study and results obtained by Feng and Michaelides.[51] A good agreement in horizontal and vertical velocity was observed; however, the vertical velocity showed fluctuations as compared to the smooth profile obtained by Feng and Michaelides[51] as these fluctuations arise due to the variability of the solid boundary due to the halfway bounceback method.

B. Flapping wings

Two-dimensional simulations using halfway bounceback LBM were carried out for a single rigid wing and two rigid wings undergoing clap and fling motion. For the purpose of performing additional validation of the methodology, instantaneous lift and drag coefficients recorded in the present study for the conditions mentioned were compared with published data.[26]

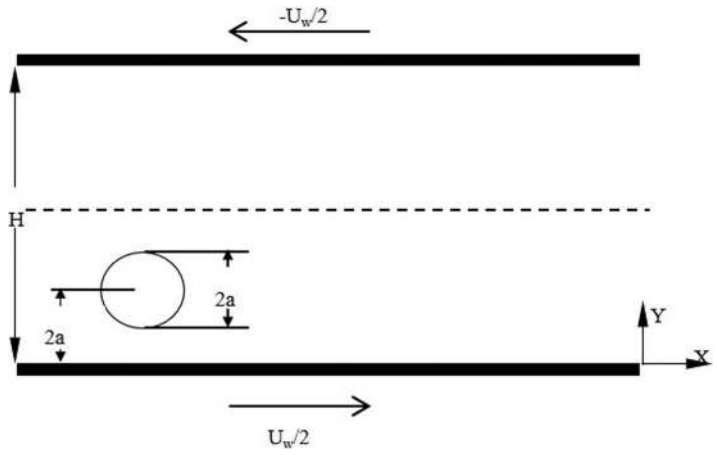

FIG. 6. A neutrally buoyant cylinder in a simple shear flow between two walls initially placed at y = 0.25 H.

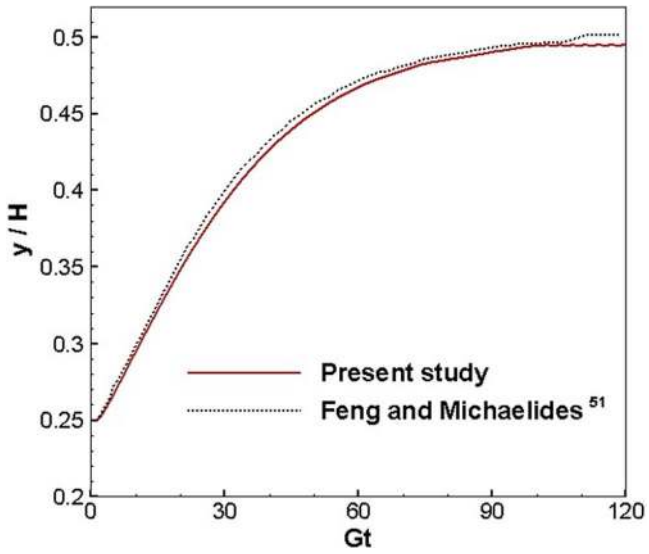

FIG. 7. Non-dimensional vertical position of the cylinder versus non-dimensional time Gt.

1. Test for convergence

A computational domain of size $20C \times 20C$ (C is the chord length) was taken for single wing simulations, whereas for two wings the size of domain was $30C \times 30C$. A pictorial representation of the computational domain is shown in Fig. 9. Periodic boundary conditions were imposed on all four boundaries of the domain. For the validation of two wing simulations δ was set as 0.1. To test for the domain independence and convergence of the numerical method employed for the two flapping wings simulations, four simulations with progressively finer spatial resolutions of 1200×1200, 1800×1800, 2400×2400, and 3000×3000 lattice nodes were considered. The variation of mean lift coefficient $\langle C_L \rangle$ with the number of lattice nodes (logarithmic scale) in the above mentioned

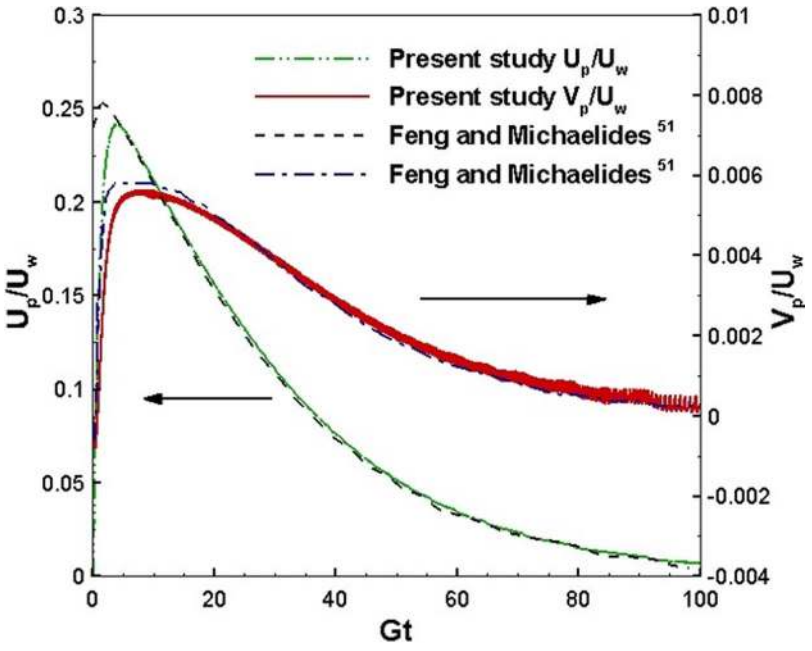

FIG. 8. Horizontal and vertical dimensionless velocities of the cylinder as a function of dimensionless time Gt.

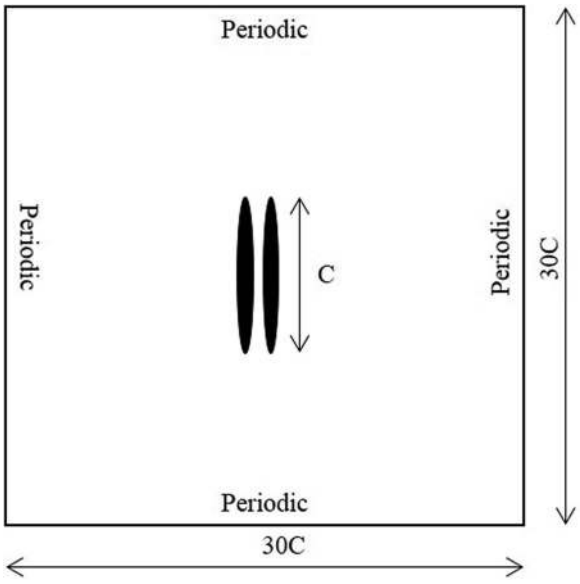

FIG. 9. Layout of the computational domain for two wing simulations with boundary conditions.

domain sizes is shown in Fig. 10 for Re = 16, $\xi = 50\%$ and $\delta = 0.1$. The mean lift $\langle C_L \rangle$ and mean drag $\langle C_D \rangle$ were calculated by time averaging the instantaneous lift and drag coefficients over one complete "clap and fling" cycle (e.g., $\langle C_L \rangle = \frac{1}{T} \int_{t_o}^{t_o+T} C_L dt$). It was observed that beyond a domain with 1800 × 1800 lattices, there was no change in $\langle C_L \rangle$ as the lattice spacing became finer. In general, the fluctuations in the instantaneous lift coefficients subsided as the number of grid points was increased. Therefore, a domain with 2400 × 2400 lattices was chosen for all further two wing simulations.

Fig. 11 shows the comparison of the lift coefficient and drag coefficient per wing of one wing and two wing "fling half stroke" for Re = 16 and $\xi = 50\%$, respectively, between the present study and Miller and Peskin.[26] The "fling half stroke" for this validation and the subsequent discussion excluded the deceleration and rotation portion of the downstroke as prescribed by Miller and Peskin[26] in their paper. The results obtained show good agreement both qualitatively and quantitatively. A

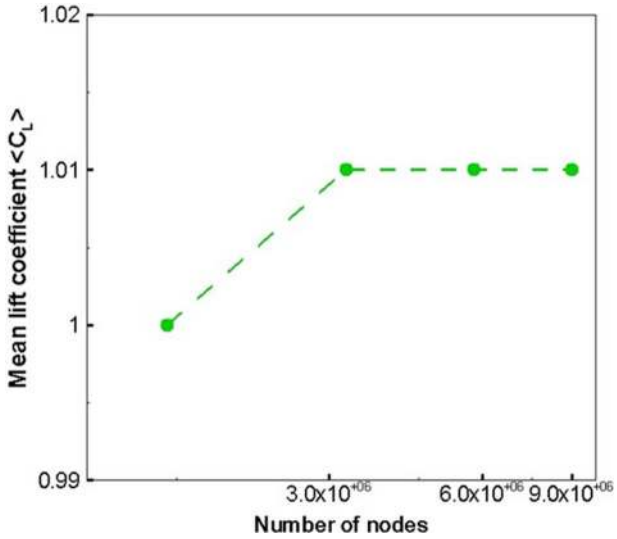

FIG. 10. Test for domain independence of mean lift coefficient $\langle C_L \rangle$.

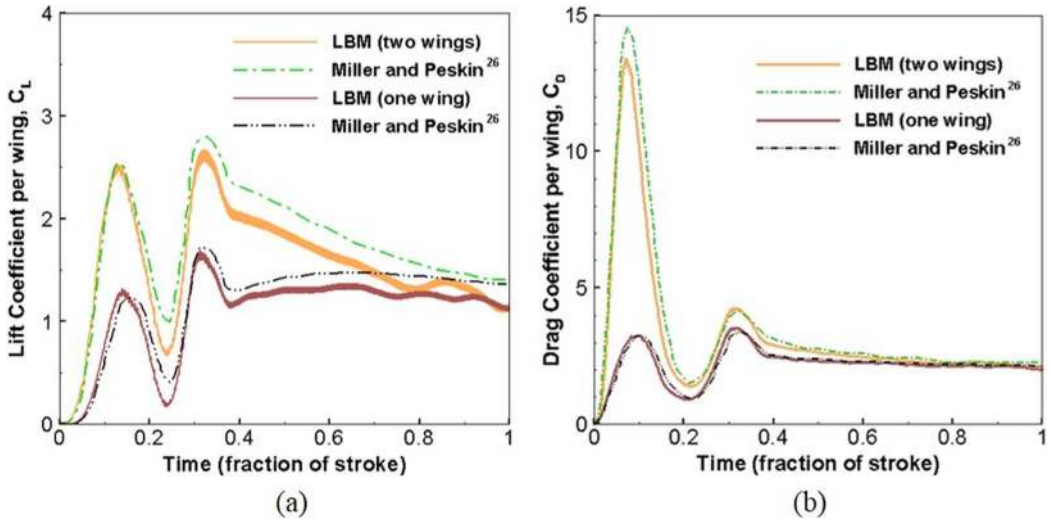

FIG. 11. Variation of (a) Lift coefficient and (b) Drag coefficient per wing with time for fling half stroke for Re = 16 compared against Miller and Peskin.[26]

moving average method, that resulted in change in average force coefficients by $<10^{-3}\%$, has been used to reduce fluctuations and smoothen the force history over the entire simulation period. One of the reasons that directly contributes to these fluctuations was the fact that certain grid points undergo transitions from non-fluid region to fluid region or vice versa due to movement of the solid. Thus, the number of fluid nodes is not conserved and the volume occupied by the solid object varies. A few earlier studies have also reported such oscillations in their force measurements pertaining to the moving boundary using LBM.[35,52]

The first peak in the lift coefficients corresponds to the lift forces generated during wing rotation, whereas the second peak corresponds to the period of translational acceleration. During the early phase of rotation and translation, the lift coefficient per wing for the two wing simulation is almost twice of that obtained with a single wing. It is only during the later stages of the translation phase that the lift for a single wing simulation catches up with that of the two wings simulation. The *Wagner Effect* is liable for this delay in the development of lift of the single wing. However, the two wing system overcomes this effect when the starting vortices are eliminated, which causes the bound vortex to form quickly resulting in a high lift at the very beginning of the downstroke.

V. RESULTS AND DISCUSSION

In this section, results obtained by numerical simulation of flapping wings employing "clap and fling" motion have been presented and discussed. The wings were assumed to be rigid and elliptical in shape. Simulations for aspect ratios of 10, 20, and 40 were performed and lift behavior examined, which are shown in Fig. 12. The variation in instantaneous lift with change in aspect ratio is negligible, hence, an aspect ratio of 10 was chosen for all simulations presented in this paper.

A. Roles of key flapping parameters

To study the role of kinematic parameters on flight performance, the impact of translational rotational overlap ξ, the gap between two wings δ and Reynolds number Re on the lift and drag behavior for a complete "clap and fling" cycle was examined. In the present study, rather than examining mean drag $\langle C_D \rangle$, emphasis has been placed on analyses of the evolvement of mean lift $\langle C_L \rangle$ by varying kinematic parameters, as the main objective of this study was to maximize lift. Re was varied from 8 to 128, with the minimum Re intended to emulate the smallest insect employing the same kinematics[26] and ξ was varied from 0% to 100%. From physiological constraints, the

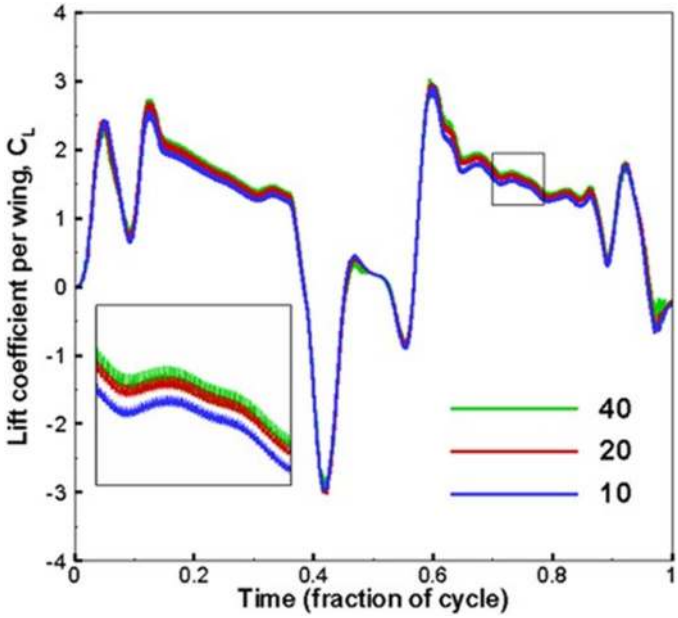

FIG. 12. Lift coefficient as function of time for complete cycle for Re = 16, ξ = 50%, and δ = 0.1 with different aspect ratios. Inset shows the enlarged view of the window.

minimum distance between wings at the end of clap stroke for any insect is not expected to be more than one-fourth of the wing chord. Any value of the separation beyond this value is anticipated to be of little value to the overall generation of lift. Hence, δ was chosen to lie between 0 and 0.25.

1. *Effect of overlap* ξ

The impact of ξ on mean lift and drag per cycle was investigated by analysis of the variation of $\langle C_L \rangle$ and $\langle C_D \rangle$ at a constant Re and δ with ξ ranging from 0% to 100%. Fig. 13(a) shows the time averaged lift coefficient $\langle C_L \rangle$ versus overlap ξ (the time averaged drag coefficient $\langle C_D \rangle$ versus overlap ξ is shown in the inset) for Re = 16 and Re = 128 with the gap kept constant at δ = 0.1. As

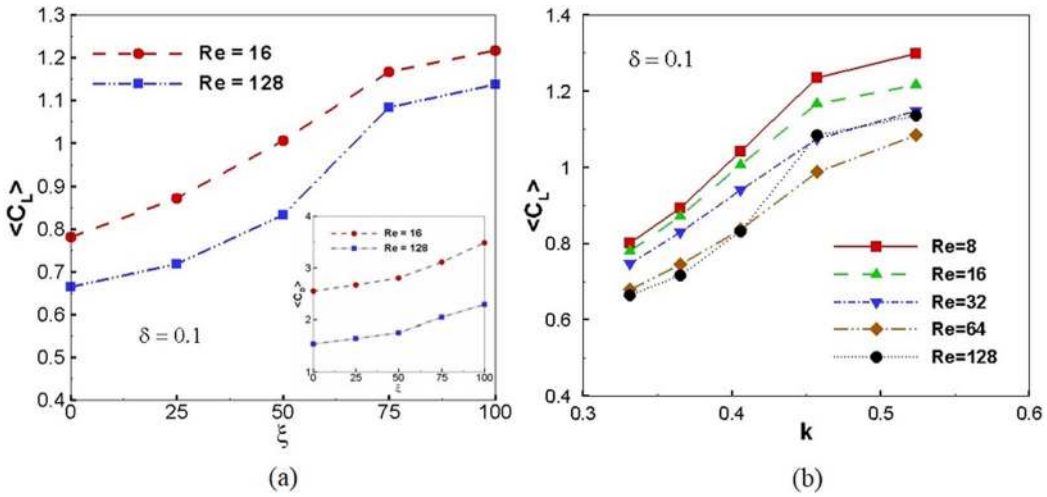

FIG. 13. Variation in average lift coefficient $\langle C_L \rangle$ with (a) change in overlap ξ for Re = 16 and Re = 128 with δ = 0.1, and (b) reduced frequency k for different Re with δ = 0.1. Also shown in inset of (a) is the average drag coefficient $\langle C_D \rangle$.

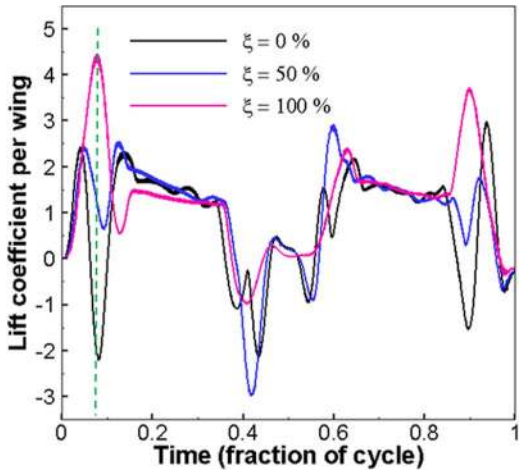

FIG. 14. Lift coefficient per wing as function of time for one complete cycle for Re = 16 and $\delta = 0.1$ with different overlaps.

is evident from this figure, the increase in overlap results in an appreciable increase in lift as well as drag.

In Fig. 13(a), for Re = 16 the mean lift $\langle C_L \rangle$ grew from 0.781 at $\xi = 0\%$ to 1.216 at $\xi = 100\%$. Similarly, for Re = 128 with ξ varying from 0% to 100%, an increase of 71.2% in $\langle C_L \rangle$ was registered. Analogous behavior in variation of lift with ξ was observed for other values of δ as well. This clearly indicates that the impact of parameter ξ in lift enhancement is more significant at higher Re. In addition, the average drag coefficient increased by 36.8% and 48.5% for Re = 16 and Re = 128, respectively.

Fig. 13(b) shows the variation in $\langle C_L \rangle$ with reduced frequency k for all Re with $\delta = 0.1$. Scaling arguments indicate that, for a wing in forward flapping flight, the mean lift varies nonlinearly with reduced frequency ($\langle C_L \rangle \sim k^2$),[4,53] although for clap and fling kinematics no such relationship has been defined in literature. As shown in Fig. 13(b), the current results also indicate that the mean lift is a nonlinear function of the reduced frequency in the range of k between 0.33 and 0.52.

To understand the increase in $\langle C_L \rangle$ with ξ, the instantaneous time-dependent lift coefficients were examined and are shown in Fig. 14 for $\xi = 0\%$, 50%, and 100% for Re = 16 with $\delta = 0.1$. The effect of overlap ξ could be identified from the peak values of instantaneous lift coefficient during pronation and supination periods. For $\xi = 0\%$, the wing starts to translate only after it has completed the rotational phase and has reached the desired angle of attack. Hence, there are two separate peaks corresponding to lift generated during wing rotation and translational acceleration. As shown in Fig. 14 for $\xi = 0\%$ and $\xi = 50\%$, during the beginning of fling when the wing pronates, lift coefficient increases until the wing stall occurs resulting in the decrease in lift (for $\xi = 0\%$ it falls to a negative value). It rises again due to translational acceleration (or dynamic stall) and hence a second maximum is obtained. However, for $\xi = 100\%$, wing rotation and acceleration begin at the same time instant, and therefore instead of two separate peaks, corresponding to wing rotation and translational acceleration, one single peak of magnitude greater than the sum of the two individual peaks is obtained. Similar crests and troughs in instantaneous lift are seen for the clap-half stroke as well during the wing supination.

In aid of the above explanation on the behavior of lift, vorticity around the wings is plotted at fraction of cycle of 0.09 (marked by a dotted line in Fig. 14) for $\xi = 0\%$ and 100% in Figs. 15(a) and 15(b), respectively. For 0% overlap, it is seen that the leading edge vortex (LEV) formed at the beginning of rotation is shed, characterized by the negative peak in instantaneous lift. While at the same instant for 100% overlap, the LEV formed at the start of rotation grows stronger as the wing begins to accelerate before the wing stall could happen and a peak in lift is registered. Thus, it is inferred that as the overlap increases, the gap between the start of rotation and translation narrows resulting in a continuous increase in lift. The contribution from lift generation mechanisms:

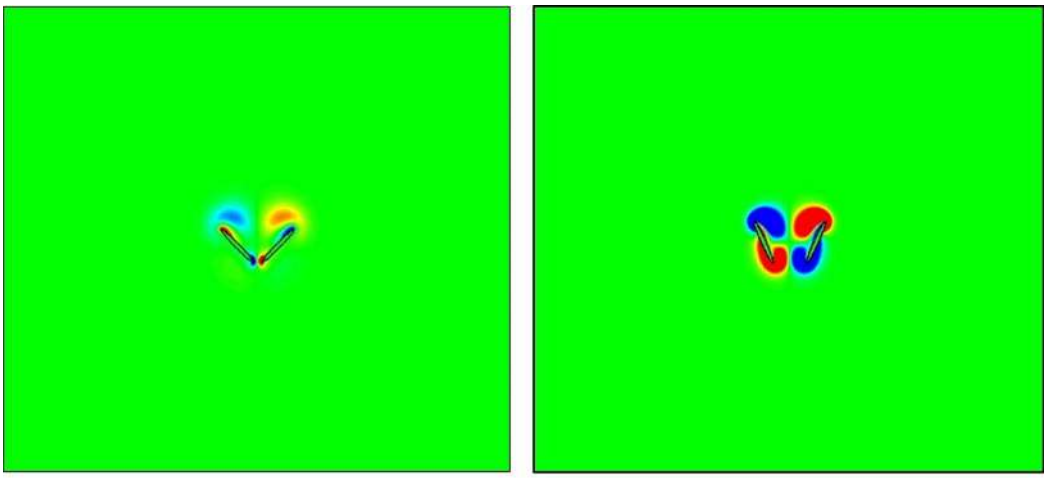

FIG. 15. Vorticity around the wings with (a) $\xi = 0\%$ and (b) $\xi = 100\%$ for Re $= 16$ and $\delta = 0.1$ at fraction of cycle $= 0.09$. Lighter gray and darker gray (red and blue colors) indicate anti-clockwise (out of the plane of paper) and clockwise rotation (into the plane of paper), respectively.

rotational effect and delayed stall supplement each other more effectively to a greater extent with increase in overlap, which eventually leads to higher lift.

Moreover, as visible in Fig. 14, not only does the magnitude of negative peaks decrease with an increase in ξ, the duration of the cycle for which the instantaneous lift remains below zero also reduces considerably. This factor also contributes in enhancing the mean lift with increase in ξ. Therefore, the translational-rotational overlap factor ξ plays a pivotal role in lift augmentation in the clap and fling kinematics.

It has been reported that formation of a jet downstream of the flapping airfoils is responsible for the generation of an opposite reaction force.[54–56] The time averaged downwash velocity (non-dimensionalized by maximum translational velocity), recorded for one complete cycle at a distance of $0.125C$ downstream of the trailing edge, for different overlaps is shown in Fig. 16. As the downwash velocity is shown to be increasing with an increase in overlap ratio, it is clear that the maximum lift will be produced for $\xi = 100\%$ which is in agreement with results shown in Fig. 13.

2. Effect of Re

The effect of Reynolds number on the mean lift and drag coefficients during the entire clap and fling stroke has been studied. Fig. 17 shows the time averaged lift coefficient for various Re (the time averaged drag coefficient versus Re is shown in inset). The spacing between the wings was chosen as $\delta = 0$ and $\delta = 0.25$, and overlap factor was kept constant at $\xi = 50\%$. As is evident from Fig. 17, for $\delta = 0$, $\langle C_D \rangle$ decreases rapidly from Re $= 8$ to Re $= 64$ beyond which the drop is gradual; however, for $\delta = 0.25$, the drag coefficient decreases moderately till Re $= 32$, beyond which it remains nearly constant. This drop in $\langle C_D \rangle$ with increase in Re could be attributed to the large effect of added mass at lower Re. As Re decreases, viscous forces become even more dominant as the width of the boundary layer around the wing grows and the mass of fluid entrained by the wing increases. Moreover, the acceleration of the wing creates a larger reaction force due to the accelerated fluid. Therefore, a larger drag is encountered at lower Re.

The variation in average lift coefficient as a function of Re shows an interesting phenomenon. As is shown in Fig. 17, starting from Re $= 8$, $\langle C_L \rangle$ decreases with increase in Re, reaches a minimum at Re $= 84$ and then increases till Re $= 128$. The increase in lift coefficient from the point of minimum was more prominent at $\delta = 0$ than at $\delta = 0.25$.

Another important revelation about the variation of lift with Re is that the concave nature of the curve is obtained only for $\xi > 25\%$. Whereas for $\xi < 25\%$, the lift is a decreasing function of

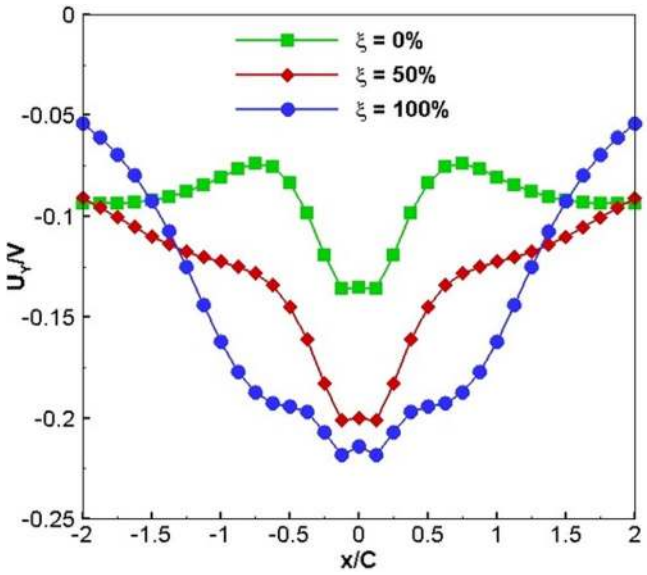

FIG. 16. Time averaged dimensionless downwash velocity profile for Re = 16 and $\delta = 0.1$ with different overlaps at $0.125C$ downstream of the trailing edge.

Re. Thus, the increasing nature of the mean lift coefficient also depends on overlap ξ. In fact, it was observed that after the minima was achieved at $\xi = 50\%$, the rise in lift till Re = 128 was 7.3%. For $\xi = 75\%$ and 100%, the increase recorded was 12.2% and 4.1%, respectively (δ was 0 for all these comparisons). This implies that the overlap together with the Reynolds number plays a key role in lift enhancement.

To identify the reason for this increase in mean lift with Re, the instantaneous time varying lift coefficients for a range of Re as shown in Fig. 18 are analyzed. On observation, it is clear that the instantaneous lift for Re = 128 is always smaller than that of Re = 8. However, for Re $\geq$ 64 the variation of instantaneous lift coefficient differs from that of Re $\leq$ 32 near the beginning of the upstroke (i.e., τ/T $\geq$ 0.5 where τ is the time instant and T is the time period for one cycle). The key difference in the magnitude of instantaneous lift occurs at the time instant of τ/T = 0.64 (marked by

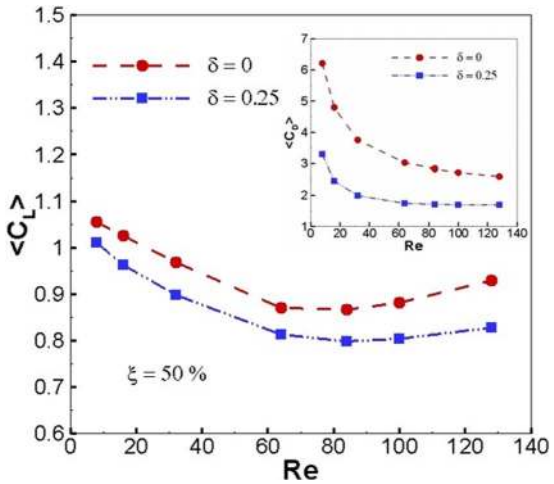

FIG. 17. Variation in average lift coefficient $\langle C_L \rangle$ and average drag coefficient $\langle C_D \rangle$ (inset) with change in Re with $\delta = 0$ and $\delta = 0.25$ for $\xi = 50\%$.

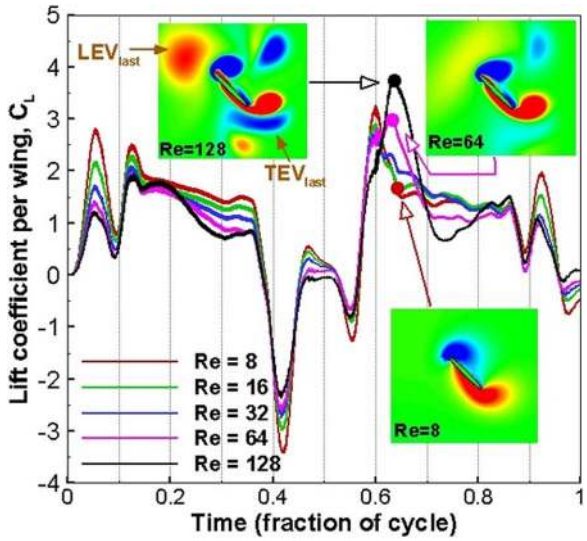

FIG. 18. Lift coefficient per wing as function of time for one complete cycle with $\delta = 0.25$ and $\xi = 50\%$ for different Re. The insets show the vorticity contours around the right wing at τ/T = 0.64 for Re = 8, 64, and 128. Also labelled are the leading and trailing edge vortices shed during the last half-stroke (LEV_{last} and TEV_{last}, respectively) and their interaction with the wing.

dots in Fig. 18) where the magnitude of peaks corresponding to Re of 64 and 128 are significantly higher than that of Re of 8 (for Re = 128, the lift is more than twice that of Re = 8). Also shown in the inset in Fig. 18 are the contours of vorticity around the right wing at τ/T = 0.64 for Re = 8, 64, and 128. These inset images show that the difference in mean lift could be due to the interaction of the wing with the vortices (marked as LEV_{last} and TEV_{last}, where "last" means the earlier half stroke) as shown in the figure.

As pointed out in the earlier paragraph and in Figs. 17 and 18, it appears that the increase in mean lift observed for Re $\geq$ 84 could be due to the reason that the time-averaged lift during either fling or clap half strokes may show a non-monotonous variation with an increase in Re. Hence, the mean lift coefficients for (a) fling, and (b) clap half strokes have been separately listed in Table I at different Re (note that the mean lift for the entire cycle is the average of lift recorded for clap and fling half stokes). From Table I, it is clear that the mean lift during fling half stroke decreases monotonically with an increase in Re. Second, for all Re the mean lift during the clap half stroke is higher than its fling half stroke and the difference between the two keeps increasing with increase in Re. It is also evident from Fig. 18 that the instantaneous lift coefficient for Re = 128 is predominantly lower than Re = 8, except near $\tau / T = 0.64$ where the peak for the

TABLE I. Mean lift coefficients for fling and clap half strokes at different Re for $\xi = 50\%$ and $\delta = 0.25$.

Re	$\langle C_L \rangle$	
	Fling half stroke	Clap half stroke
8	0.97	1.05
16	0.86	1.07
32	0.73	1.06
64	0.61	1.02
84	0.58	1.02
100	0.57	1.03
128	0.58	1.08

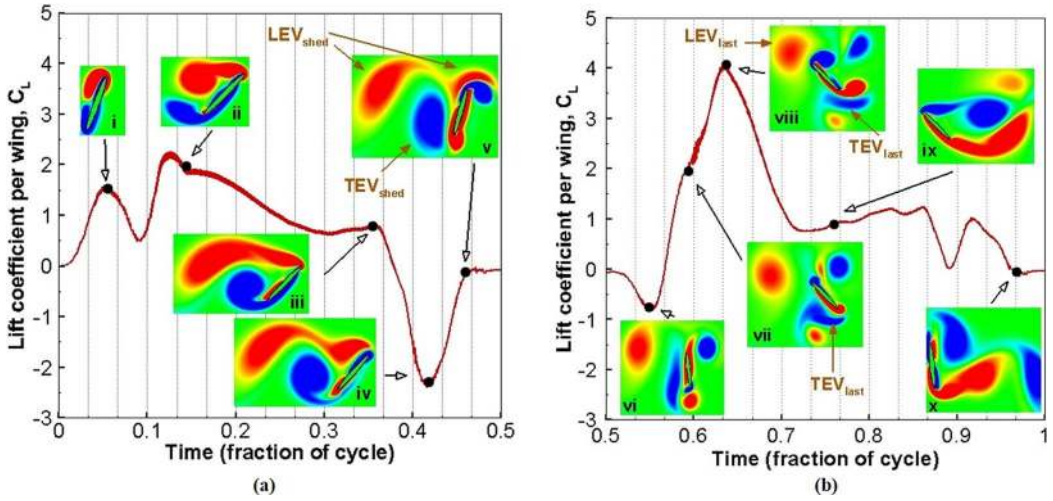

FIG. 19. Lift coefficient per wing (C_L) as a function of dimensionless time for (a) fling-and (b) clap half stroke for Re = 128 with $\xi = 50\%$ and $\delta = 0.1$. The insets show the vorticity contours around the right wing at time instants corresponding to the wing positions shown in Fig. 4(i)–(x).

former case is highest. Hence, it can be concluded that this peak contributes to the increase in mean lift for the clap half stroke, and thereby to the mean lift for the entire cycle as appears in Fig. 17. This peak in instantaneous lift is attributed to the fact that as the upstroke begins, the wings interact with the wake shed during the fling stroke (labelled as LEV_{last} and TEV_{last}). This unsteady mechanism, known as "wing-wake interaction," produces aerodynamic lift by the transfer of fluid momentum to the wing, thus increasing the effective flow speed surrounding the wing and enhancing lift. During the upstroke and for Re = 128, the interaction with the wake first occurs at the trailing edge whose rotation is opposite to that of the existing attached TEV. As a result, there is an increase in the net circulation around the wings which leads to an increase in lift. This phenomenon is not discernible for Re $\leq$ 32, since the vortices shed during the fling stroke rapidly dissipate due to the large viscous effects (especially for Re = 8). Contrary to the TEV, the LEV shed from previous stroke has an opposite direction to the attached LEV which has a role in the sudden decrease in instantaneous lift beyond $\tau / T = 0.64$.

As a representative case, the lift coefficient per wing as a function of dimensionless time for clap and fling half strokes is shown separately in Figs. 19(a) and 19(b), respectively, for Re = 128, $\xi = 50\%$, and $\delta = 0.1$. With reference to Fig. 19(a), at the beginning of fling (i)–(ii), a strong leading edge vortex and a weak trailing edge vortex is formed, thereby increasing the lift. The two peaks correspond to the lift generated during (i) rotation, and (ii) translational acceleration before the shedding of corresponding LEV. As the wing translates, the trailing edge vortex grows and the LEV is about to be shed, thus a gradual drop in lift is registered (ii)–(iii). At (iii), the wing begins to decelerate and there is a sharp decrease in lift and the LEV is shed (iv). At (iv), rotation begins and a new LEV of opposite rotation is formed around the wing that grows stronger till (v), indicating the increase in lift. Also, at (v) the TEV is shed and a new TEV forms.

As shown in Fig. 19(b), at the beginning of clap (vi), the LEV formed in (v) is shed during the rotation phase resulting in a reduction in lift. As the translation begins (vii), a new LEV and TEV begins to form and the wing moves back through its wake. The LEV is very weak in comparison to the lift generated, and this high lift is accredited to the interaction of the wing with the previously shed TEV whose rotation is of the same sense as that of attached LEV. This interaction continues and lift keeps rising until (viii) when the wing interacts with the earlier shed LEV whose rotation is of opposite sense to the lift generating circulation around the wing, and there is a sharp decline in lift as it moves through this wake. Subsequently, as the wing moves back, the LEVs are shed and the trailing edge vortices grow (ix) resulting in a reduction in lift. Beyond (ix), the lift drops as the wings decelerate. It increases again due to the rotational motion and then drops again as the wing

stalls. Finally at (x), the LEVs and TEVs formed during rotation are shed, and the lift begins to rise again as the fluid squeezed between two wings is expelled out giving an additional thrust.

Thus, it can be concluded that with an increase in Re, the wake-capture mechanism becomes dominant, thereby proving that the "wing-wake interaction" is crucial to lift enhancement in the clap-and-fling motion.

A comparison of these flow structures shown in Fig. 19 with the particle image velocimetry (PIV) results of Clercq *et al.*[57] and Croon *et al.*[58] for "DELFLY" (which is an insect flight inspired MAV that operates on the "clap and peel" mechanism) shows qualitative agreement. In particular Croon *et al.*[58] also showed the presence of strong leading and weak trailing edge vortices in the early part of downstroke. The "fling" phase for the "DELFLY" was slightly different from the one described above for rigid wings. Since the wings of their flyer were flexible, they deform on interacting with the fluid which made them tear apart and hence was called "peel" (the flexible fling). They analyzed the flow field around the wings of the "DELFLY" by PIV and force measurements on the wings were also performed simultaneously. Their force measurements indicated a high peak value in lift force during the "peel" phase which was explained to be the consequence of annihilation of trailing edge vortices, since there was no hindrance in the buildup of circulation around the wings.[57] Although the "DELFLY" used flexible membranes and the Reynolds number operating range was O(10^4), which is quite high in comparison to the typical insect flight/present study, the fluid dynamics that originates from the flapping of the wings is anticipated to be at par with that of insect flight.[57]

A preliminary analysis on the effect of using an airfoil with sharp trailing and rounded leading edges was also performed. Two cases were simulated using NACA0010 airfoil for Re = 16 and Re = 128 with $\xi = 50\%$ and $\delta = 0.1$ and the thrust generated was compared with that of the elliptical airfoil. For Re = 16, the $\langle C_L \rangle$ for the elliptical airfoil and NACA0010 was recorded as 1.006 and 1.03, respectively. For the case of Re = 128, $\langle C_L \rangle$ was recorded to be 0.834 and 0.922, respectively. This signified an increase in mean lift due to the use of an airfoil with sharp and rounded edges of 2.4% and 10.5% for Re of 16 and 128, respectively. However, our focus in this study is not on delineating the effect of sharp or rounded leading and trailing edges on the lift-drag behavior; hence, a much more detailed analysis on this aspect will be pursued in the future.

3. Effect of gap δ

We now discuss the effect of gap δ, for a fixed Re and ξ, on the generation of time averaged lift and drag per cycle.

For two overlaps of $\xi = 25\%$ and 75% and Reynolds number of 64, the variation in $\langle C_L \rangle$ and $\langle C_D \rangle$ (inset) with change in δ is shown in Fig. 20. The results from simulations reveal that as the

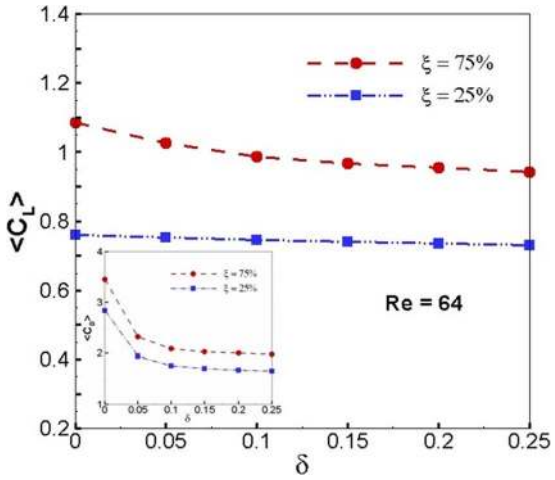

FIG. 20. Variation in average lift coefficient $\langle C_L \rangle$ and average drag coefficient $\langle C_D \rangle$ (inset) with change in gap $\delta$for $\xi = 25\%$ and $\xi = 75\%$ for Re = 64.

gap between two wings increases, both $\langle C_L \rangle$ and $\langle C_D \rangle$ decrease. This is consistent with an earlier study,[28] where instantaneous lift was shown to be higher for $\delta = 0$ against $\delta = 1/6$ for Re = 128. The decrease in $\langle C_D \rangle$ is more significant and prominent as compared to $\langle C_L \rangle$. The drop in $\langle C_D \rangle$ was 43% for both the overlaps, as δ varied from 0 to 0.25. As far as lift is concerned, $\langle C_L \rangle$ decreased by 13.2% at $\xi = 75\%$ in comparison to 3.9% at $\xi = 25\%$, clearly indicating that the lift coefficient is more sensitive to overlap ratio at higher values of this parameter, in contrast to the drag coefficient where the drop is nearly the same for both overlaps. The reason for the reduction in $\langle C_D \rangle$ and $\langle C_L \rangle$ with increasing separation could be attributed to the fact that it is only during the last stages of upstroke and initial stages of downstroke (i.e., time duration when the two wings undergo rotation about their leading or trailing edges performing the "pronation") that the instantaneous drags and lifts vary substantially with change in gap. During the rest of the stroke, the instantaneous drag and lift profiles do not show any change with a change in initial gap. This variation in the instantaneous lift and drag during early fling and later clap phase occurs due to the phenomenon known as wing-wing interaction[21] where the closeness of the wings ensures that no TEVs are generated during the fling.

Although the range of δ in the results discussed so far was taken as 0–0.25, additional simulations were performed for δ extending beyond the prescribed range, i.e., till $\delta = 2$, to investigate the possibility of a limiting case where the lift stagnates to a constant value. It was observed that for $\delta > 0.5$, $\langle C_L \rangle$ remained constant and approached that obtained in the case of a single wing, which is consistent with $\delta > 0.8$ which was reported for Re = 15.3 using three-dimensional simulations.[27] This indicates that beyond $\delta = 0.5$, both wings behave as two separate individual entities performing the upstroke/downstroke motion in complete isolation, without any influence on their respective circulations due to the presence of the neighboring wing in vicinity.

It can hence be inferred that "clap and fling" is effective in lift generation only when the two wings come as close as possible to each other. As the separation between the wings increases, the *Wagner Effect* starts to dominate again and lift decreases to that of the single wing.

B. Surrogate analysis

Surrogate-based model construction and analysis has been carried out to establish the relationship between the dependent variable, i.e., mean lift ($\langle C_L \rangle$) and the independent variables, i.e., parameters δ, ξ, and Re. This reduced-order model formulation provides global perspective and impact on mean lift that cannot be obtained by individually varying each of the kinematic variables. Over 160 numerical simulations were performed to obtain a second-order polynomial function for mean lift ($\langle C_L \rangle$), thereby assisting in understanding how each parameter influences $\langle C_L \rangle$. The equation obtained through surrogate modeling is

$$\begin{aligned}\langle C_L \rangle = 0.868 - 5.62 \times 10^{-3}\mathrm{Re} - 0.328\delta + 6.43 \times 10^{-3}\xi + 3.93 \times 10^{-5}\mathrm{Re}^2 + \\ 1.50 \times 10^{-4}\mathrm{Re}\delta + 3.07 \times 10^{-6}\mathrm{Re}\xi + 1.11\delta^2 - 7.82 \times 10^{-3}\delta\xi \\ +5.92 \times 10^{-6}\xi^2\end{aligned} \tag{25}$$

with the goodness of the fit $R^2_{adj} = 0.97$.

The polynomial expression given by Eq. (25) captures the trend of mean lift curve with a minimum in the chosen range of Re. The equation also indicates that mean lift is an increasing function of overlap ξ and a decreasing function of separation δ in their respective selected ranges.

Earlier, the behavior of mean lift with all the three parameters was shown individually, with other two held constant. In order to visualize the change in mean lift with all three parameters simultaneously, a three-dimensional cuboidal surface was generated. The cuboid encloses iso-contours of $\langle C_L \rangle$ whose axes correspond to each of the design variables δ, ξ, and Re.

As shown in Fig. 21(a) where $\xi = 100\%$ plane has regions of higher lift than $\xi = 0\%$ plane, an increase in the overlap leads to an increase in the mean lift. In Fig. 21(b), with increase in separation δ from 0 to 0.25, the high lift region (as visible in $\delta = 0$ plane in lighter gray (red)) transitions to a low lift zone (darker gray (blue)). In comparison to $\delta = 0$ plane, the low lift region (darker gray

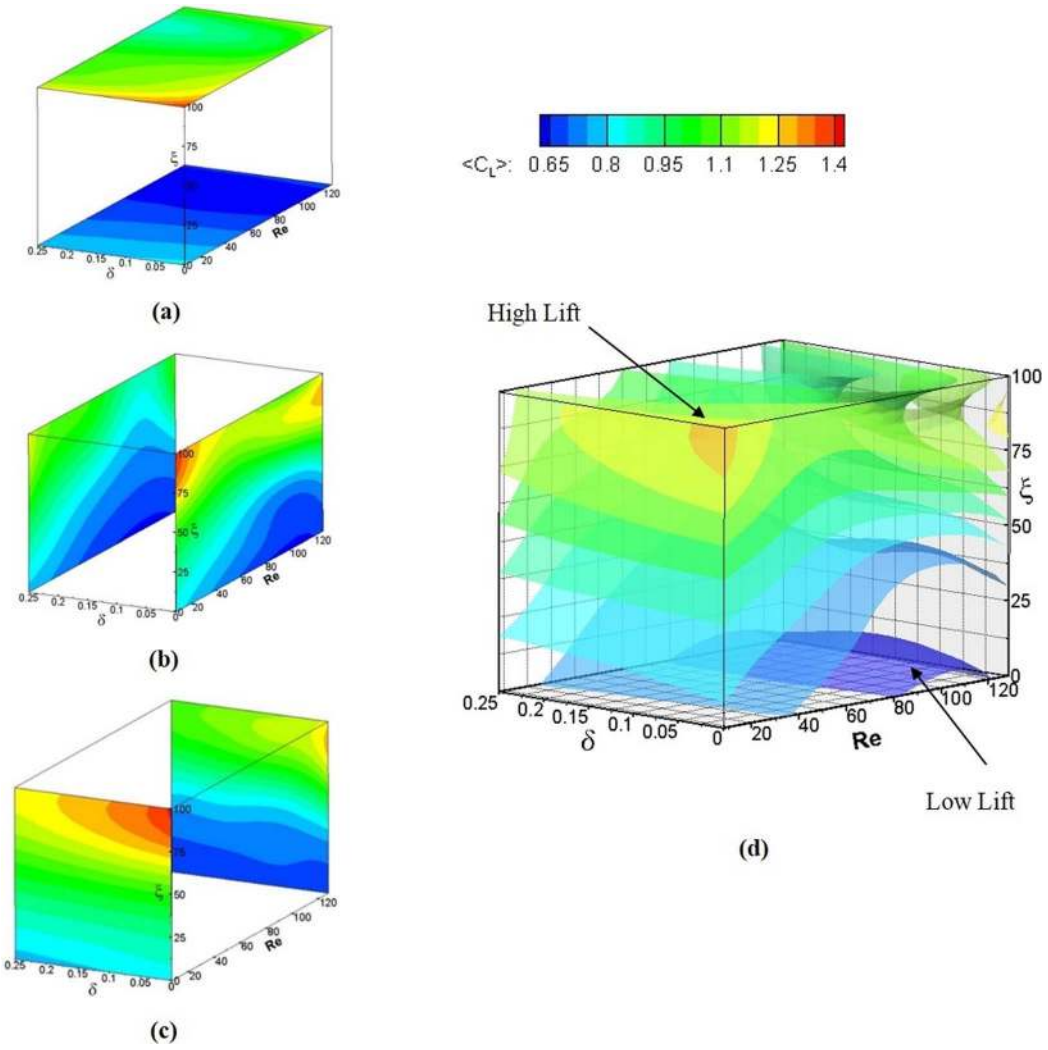

FIG. 21. Iso-contours of mean lift ($\langle C_L \rangle$) as a function of Reynolds number, percentage overlap, and separation between the wings.

(blue)) has further diffused into $\delta = 0.25$ plane, which depicts the decreasing trend of lift with gap δ. Similar conclusions can be drawn from Fig. 21(c). The complete variation of mean lift in the range of parameters selected is shown in Fig. 21(d). The highest mean lift is witnessed at the upper left corner of the cuboid, which demonstrates that the lift is maximum at low values of Re and gap δ, and high overlap ξ.

Using the surrogate model, sensitivity analysis was carried out as well. Fig. 22 shows the sensitivity indices of the three kinematic variables on $\langle C_L \rangle$. It is observed that the sensitivity of ξ is higher than the other two variables and hence has the maximum impact on $\langle C_L \rangle$ (followed by Re) indicating it to be the most crucial parameter among the three. The difference in the main and total sensitivity indices for ξ and Re is marginal (increase of 1.7% and 5.3%, respectively), implying that the coupling of these two variables with others is not significant. The gap δ has the minimum influence on mean lift and is the least important. However, for δ the total sensitivity is relatively higher than its main counterpart. This clearly indicates that for the range of δ considered in this work, the extent of coupling with the remaining variables cannot be ignored. The results shown in Sec. V A 3 also support the same claim.

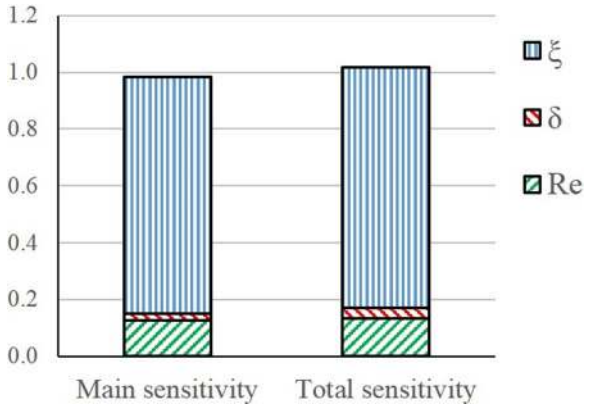

FIG. 22. Global sensitivity analysis of mean lift $\langle C_L \rangle$ showing the main and total sensitivity indices.

VI. CONCLUSIONS

The present study was directed towards quantifying the role of three kinematic parameters affecting clap and fling kinematics by the analysis of the flow dynamics associated with the flapping motion of finite-thickness wings. In this regard, the implementation of the lattice Boltzmann method to simulate moving boundary problems associated with finite thickness membranes has been demonstrated. The method was tested for a case of cylinder in simple shear flow with the results validated against earlier published data. It was shown that LBM can be used accurately to compute the total drag and lift forces on a moving object in a flow; however, fluctuation and noise in the forces were noticeable. To circumvent this, a moving average procedure was applied to reduce the fluctuations typically observed in forces.

A parametric study to analyze the lift and drag behaviors of one and two wings performing "clap and fling" motion was carried out using surrogate analysis. The parametric study carried out on flapping wings revealed that

1. With an increase in ξ, the mean lift and drag increased significantly. As the overlap increases, the gap between the start of rotation and translation narrows. Hence, before rotational stall is reached, the translation of the wing begins resulting in a continuous increase in lift. Moreover, as ξ increases, (a) the magnitude of the negative peaks of instantaneous lift and (b) the duration of cycle for which the lift coefficient falls below zero, decrease helping in enhancing the mean lift. The role of ξ in clap and fling is analogous to φ, defined as the phase difference between plunging and pitching motion in hovering kinematics,[20,31] where $\xi = 100\%$ is similar to symmetric rotation in normal hovering.
2. With increase in Re, the mean drag decreased monotonically, whereas the mean lift decreased to a minimum and increased thereafter. The drop in mean drag with increase in Re was attributed to the large effect of added mass at lower Re. The lift generation at higher Re was marked by the presence of the "wing-wake interaction" mechanism which was absent at low Re since the wake dissipated owing to higher viscous effects. In contrast to earlier studies on clap and fling,[12–15,25,26] which have reported the "fling" portion to be the major contributor in lift generation, the present study reveals that at higher Re due to "wing-wake interaction" the early phase of upstroke just after the stroke reversal also plays a substantial part in augmenting the lift.
3. With increase in separation δ, both mean lift and drag decreased. The reduction in mean drag was found to be far more pronounced and dominant as compared with reduction in mean lift. Moreover, as the separation increased beyond $\delta = 0.5$, the mean lift remained constant and approached that obtained in the case of single wing. Thus, both wings behaved as two separate single wings performing the clap-and-fling motion oblivious to each other's presence in the neighborhood.

The rectilinear motion of wings back and forth with the wing rotation that permits the same leading edge to move forward is called normal hovering. Addition of special movements ("clap" and "fling") avoids the delay in building up of lift due to *Wagner Effect* and generates the maximum lift from the outset. This study hence authenticates the mechanism proposed by "Weis-Fogh" which claims that the performance of "clap-fling" is superior to the hovering motion and is therefore employed by most of the tiny insects.

[1] B.-J. Tsai and Y.-C. Fu, "Design and aerodynamic analysis of a flapping-wing micro aerial vehicle," Aero. Sci. Tech. **13**, 383 (2009).
[2] H. Hu, A. G. Kumar, G. Abate, and R. Albertani, "An experimental study of flexible membrane wings in flapping flight," in *Proceedings of the 46th AIAA Aerospace Sciences Meeting and Exhibit*, January, 2008, Orlando, FL, USA.
[3] W. Shyy, Y. Lian, J. Tang, D. Viieru, and H. Liu, *Aerodynamics of Low Reynolds Number Flyers* (Cambridge University Press, New York, 2008).
[4] W. Shyy, H. Aono, C.-K. Kang, and H. Liu, *An Introduction to Flapping Wing Aerodynamics* (Cambridge University Press, New York, 2013).
[5] T. J. Muller, "Fixed and flapping wing aerodynamics for micro air vehicle applications," AIAA Paper 2001-195, 2001.
[6] S. A. Ansari, R. Zbikowski, and K. Knowles, "Aerodynamic modelling of insect-like flapping flight for micro air vehicles," Prog. Aero. Sci. **42**, 129 (2006).
[7] M. Platzer, K. Jones, J. Young, and J. Lai, "Flapping wing aerodynamics: Progress and challenges," AIAA J. **46**, 2136 (2008).
[8] W. Shyy, Y. Lian, J. Tang, H. Liu, P. Trizila, B. Stanford, L. P. Bernal, C. E. S. Cesnik, P. Friedmann, and P. Ifju, "Computational aerodynamics of low Reynolds number plunging, pitching and flexible wings for MAV applications," Acta Mech. Sin. **24**, 351 (2008).
[9] W. Shyy, M. Berg, and D. Ljungqvist, "Flapping and flexible wings for biological and micro air vehicles," Prog. Aero. Sci. **35**, 455 (1999).
[10] M. I. Woods, J. F. Henderson, and G. D. Lock, "Energy requirements for the flight of micro air vehicles," Aeronaut. J. **105**, 135 (2001).
[11] D. E. Alexander, *Nature's Flyers* (The John Hopkins University Press, Baltimore, 2002).
[12] T. Weis-Fogh, "Quick estimates of flight fitness in hovering animals, including novel mechanism for lift production," J. Exp. Biol. **59**, 169 (1973).
[13] M. J. Lighthill, "On the Weis-Fogh mechanism of lift generation," J. Fluid Mech. **60**, 1 (1973).
[14] T. Maxworthy, "Experiments on the Weis-Fogh mechanism of lift generation by insects in hovering flight. Part 1. Dynamics of the 'fling'," J. Fluid Mech. **93**, 47 (1979).
[15] S. P. Sane, "The aerodynamics of insect flight," J. Exp. Biol. **206**, 4191 (2003).
[16] C. P. Ellington, C. van den Berg, A. P. Willmott, and A. L. R. Thomas, "Leading-edge vortices in insect flight," Nature (London) **384**, 626 (1996).
[17] J. Birch and M. H. Dickinson, "Spanwise flow and the attachment of the leading-edge vortex," Nature (London) **412**, 729 (2001).
[18] M. H. Dickinson and K. G. Gotz, "Unsteady aerodynamic performance of model wings at low Reynolds numbers," J. Exp. Biol. **174**, 45 (1993).
[19] W. Shyy, H. Aono, S. K. Chimakurthi, P. Trizila, C. K. Kang, C. E. S. Cesnik, and H. Liu, "Recent progress in flapping wing aerodynamics and aeroelasticity," Prog. Aero. Sci. **46**, 284 (2010).
[20] M. H. Dickinson, F.-O. Lehmann, and S. P. Sane, "Wing rotation and the aerodynamic basis of insect flight," Science **284**, 1954 (1999).
[21] F.-O. Lehmann, S. P. Sane, and M. Dickinson, "The aerodynamic effects of wing-wing interaction in flapping insect wings," J. Exp. Biol. **208**, 3075 (2005).
[22] J. Tang, D. Viieru, and W. Shyy, "Effects of Reynolds number and flapping kinematics on hovering aerodynamics," AIAA J. **46**, 967 (2008).
[23] Z. J. Wang, J. M. Birch, and M. H. Dickinson, "Unsteady forces and flows in low Reynolds number hovering flight: Two-dimensional computations vs robotic wing experiments," J. Exp. Biol. **207**, 449 (2004).
[24] H. Liu, C. P. Ellington, K. Kawachi, C. Van den Berg, and A. P. Willmott, "A computational fluid dynamics study of Hawkmoth hovering," J. Exp. Biol. **201**, 461 (1998).
[25] H. Liu and K. Kawachi, "A numerical study of insect flight," J. Comput. Phys. **146**, 124 (1998).
[26] L. A. Miller and C. S. Peskin, "A computational fluid dynamics of 'clap and fling' in the smallest insect," J. Exp. Biol. **208**, 195 (2005).
[27] M. Sun and X. Yu, "Aerodynamic force generation in hovering flight in a tiny insect," AIAA J. **44**, 1532 (2006).
[28] D. Kolomenskiy, H. K. Moffatt, M. Farge, and K. Schneider, "Vorticity generation during the clap-fling-sweep of some hovering insects," Theor. Comput. Fluid Dyn. **24**, 209 (2010).
[29] D. Kolomenskiy, H. K. Moffatt, M. Farge, and K. Schneider, "The lighthill-Weis-Fogh clap-fling-sweep mechanism revisited," J. Fluid Mech. **676**, 572 (2011).
[30] D. Kolomenskiy, H. K. Moffatt, M. Farge, and K. Schneider, "Two- and three-dimensional numerical simulations of the clap-fling-sweep of hovering insects," J. Fluid. Struct. **27**, 784 (2011).
[31] P. Trizila, C. K. Kang, H. Aono, and W. Shyy, "Low-Reynolds-number aerodynamics of a flapping rigid flat plate," AIAA J. **49**, 806 (2011).
[32] J. D. Eldredge, "Numerical simulation of the fluid dynamics of 2D rigid body motion with the vortex particle method," J. Comput. Phys. **221**, 626 (2007).

[33] M. Sun and J. Tang, "Unsteady aerodynamic force generation by a model fruit fly wing in flapping motion," J. Exp. Biol. **55**, 205 (2002).
[34] Y. Liu, N. Liu, and X. Lu, "Numerical study of two-winged insect hovering flight," Adv. Appl. Math. Mech. **1**, 481 (2009).
[35] H. Aono, A. Gupta, D. Qi, and W. Shyy, "The lattice Boltzmann method for flapping wing aerodynamics," in Proceedings of the 40th AIAA Fluid Dynamics Conference and Exhibit, June 2010, Chicago, IL, USA.
[36] D. Qi, Y. Liu, W. Shyy, and H. Aono, "Simulations of dynamics of plunge and pitch of a three-dimensional flexible wing in a low Reynolds number flow," Phys. Fluids. **22**, 091901 (2010).
[37] Y. Sui, Y.-T. Chew, P. Roy, and H.-T. Low, "A hybrid immersed-boundary and multi-block lattice Boltzmann method for simulating fluid and moving-boundary interactions," Int. J. Num. Meth. Fluids. **53**, 1727 (2007).
[38] T. Gao, N.-S. Liu, and X. Lu, "Numerical analysis of the ground effect on insect hovering," J. Hydrodynamics. **20**, 17 (2008).
[39] T. Gao and X. Lu, "Insect normal hovering flight in ground effect," Phys. Fluids. **20**, 087101 (2008).
[40] A. J. C. Ladd, "Numerical simulations of particulate suspensions via a discretized Boltzmann equation. Part 1. Theoretical foundation," J. Fluid Mech. **271**, 285 (1994).
[41] S. Succi, *The Lattice Boltzmann Equation for Fluid Dynamics and Beyond* (Oxford University Press, New York, 2001).
[42] S. Chen and G. D. Doolen, "Lattice Boltzmann method for fluid flows," Annu. Rev. Fluid Mech. **30**, 329 (1998).
[43] D. Qi, "Lattice-Boltzmann simulations of particles in non-zero-Reynolds-number flows," J. Fluid Mech. **385**, 41 (1999).
[44] X. He and L.-S. Luo, "Theory of the lattice Boltzmann method: From the Boltzmann equation to the lattice Boltzmann equation," Phys. Rev. E. **56**, 6811 (1997).
[45] R. Mei, L.-S. Luo, and W. Shyy, "An accurate curved boundary treatment in the lattice Boltzmann method," J. Comput. Phys. **155**, 307 (1999).
[46] R. Mei, D. Yu, W. Shyy, and L.-S. Luo, "Force evaluation in the lattice Boltzmann method involving curved geometry," Phys. Rev. E. **65**, 041203 (2002).
[47] N. V. Quiepo, R. T. Haftka, W. Shyy, T. Goel, R. Vaidyanathan, and P. K. Tucker, "Surrogate-based analysis and optimization," Prog. Aero. Sci. **41**, 1 (2005).
[48] W. Shyy, N. Papila, R. Vaidyanathan, and K. Tucker, "Global design optimization for aerodynamics and rocket propulsion components," Prog. Aero. Sci. **37**, 59 (2001).
[49] W. Shyy, Y.-C. Cho, W. Du, A. Gupta, C.-C. Tseng, and A. M. Sastry, "Surrogate-based modeling and dimension reduction techniques for multi-scale mechanics problems," Acta Mech. Sin. **27**, 845 (2011).
[50] A. Gupta, J. H. Seo, X. Zhang, W. Du, A. M. Sastry, and W. Shyy, "Effective transport properties of LiMn2O4 electrode via particle-scale modeling," J. Electrochem. Soc. **158**, A487 (2011).
[51] Z. G. Feng and E. E. Michaelides, "The immersed boundary-lattice Boltzmann method for solving fluid-particles interaction problems," J. Comput. Phys. **195**, 602 (2004).
[52] P. Lallemand and L.-S. Luo, "Lattice Boltzmann method for moving boundaries," J. Comput. Phys. **184**, 406 (2003).
[53] A. Gogulapati, P. P. Friedmann, E. Kheng, and W. Shyy, "Approximate aeroelastic modelling of flapping wings in hover," AIAA J. **51**, 567 (2013).
[54] P. Freymuth, "Thrust generation by an airfoil in hover modes," Exp. Fluids **9**, 17 (1990).
[55] J. C. S. Lai and M. F. Platzer, "Characteristics of a plunging airfoil at zero freestream velocity," AIAA J. **39**, 531 (2000).
[56] K. D. Jones, C. J. Bradshaw, J. Papadopoulos, and M. F. Platzer, "Bio-inspired design of flapping-wing micro air vehicles," Aeronautical J. **109**, 385 (2005).
[57] K. M. E. De Clercq, R. De Kat, B. Remes, B. W. Van Oudheusden, and H. Bijl, "Aerodynamic experiments on DelFly II: Unsteady lift enhancement," Int. J. Micro Air Veh. **1**, 255 (2009).
[58] G. C. H. E. de Croon, M. A. Groen, C. De Wagter, B. Remes, R. Ruijsink, and B. W. van Oudheusden, "Design, aerodynamics and autonomy of the Delfly," Bioinspir. Biomim. **7**, 025003 (2012).